FERMILAB-THESIS-2025-13

Measurement of ν_μ CC Interactions With Two-Proton Final State in MINERvA

A DISSERTATION PRESENTED
BY
VLADYSLAV S. SYROTENKO
TO
THE DEPARTMENT OF PHYSICS AND ASTRONOMY

IN PARTIAL FULFILLMENT OF THE REQUIREMENTS
FOR THE DEGREE OF
DOCTOR OF PHILOSOPHY
IN THE SUBJECT OF
PHYSICS

TUFTS UNIVERSITY
MEDFORD, MASSACHUSETTS
OCTOBER 2025

Thesis advisor: Professor Hugh R. Gallagher Vladyslav S. Syrotenko

Measurement of ν_μ CC Interactions With Two-Proton Final State in MINERvA

Abstract

This dissertation presents a measurement of charged–current (CC) muon–neutrino interactions with exactly two protons and no pions in the final state (CC $2p\,0\pi$), using data collected by the MINERvA detector in the NuMI medium–energy beam at Fermilab. Such two–proton topologies are a sensitive probe of nuclear dynamics in the few–GeV regime, including multi–nucleon correlations (npnh, notably $2p2h$) and intranuclear final–state interactions (FSI) such as pion absorption and nucleon rescattering. A precise experimental characterization of these processes is essential both for neutrino–interaction theory and for reducing systematic uncertainties in oscillation experiments that rely on accurate modeling of neutrino–nucleus interactions.

Events are selected by requiring a ν_μ CC interaction with a reconstructed μ^- and two proton tracks originating from a common vertex in MINERvA's finely segmented scintillator tracker, with no reconstructed mesons. Muon charge and momentum are constrained by matching to the MINOS Near Detector, while proton identification exploits energy–loss profiles and stopping–proton features. Backgrounds from pion–producing channels that enter the signal region through FSI or reconstruction effects are constrained with data–driven sidebands (Michel–electron and isolated–cluster "blob" samples) and tuned via a simultaneous fit across signal and sideband regions.

To correct detector resolution and acceptance effects, the analysis employs iterative Bayesian unfolding with extensive validation: statistical pseudo–experiments, and robustness checks against

generator systematic "universes" and additional strong shape warps. Single–differential cross sections are reported for three observables tailored to the two–proton final state: the opening–angle cosine $\cos(\theta_{pp})$, the leading–proton momentum, and the subleading–proton momentum. Systematic uncertainties include contributions from neutrino flux, interaction modeling (e.g., npnh and resonance parameters, pion FSI), and detector response (calibration, reconstruction efficiencies).

The resulting distributions provide targeted constraints on the interplay of multi–nucleon dynamics and FSI that shape CC $2p\,0\pi$ final states on hydrocarbon. Comparisons to modern GENIE–based simulations highlight kinematic regions where model components require refinement. These measurements thus inform generator tuning and improve the reliability of neutrino–energy reconstruction strategies for current and future long–baseline oscillation programs.

Contents

Listing of figures

To my children

Acknowledgments

I wish to express my sincere gratitude to all who have, in different ways, shaped and supported the work that has led to this dissertation.

My foremost thanks go to Prof. Hugh R. Gallagher, whose guidance, patience, and thoughtful example have been central to my development as a researcher. His way of offering direction without constraint, and his understanding of the balance between scholarship and life beyond it, made this work possible. I remain grateful for his calm counsel and steady confidence at every stage of my study.

I am also thankful to Prof. W. Anthony Mann and Prof. Jeremy M. Wolcott, whose presence in research meetings and thoughtful engagement in discussions over the years have contributed greatly to the evolution of this work. Their insights and questions during presentations and conversations often helped to clarify ideas and refine my approach.

Within the MINERvA Collaboration, I have been fortunate to learn from many colleagues whose knowledge and kindness have left a lasting impression. I am especially grateful to Prof. Kevin S. McFarland, whose broad perspective and guidance were foundational; to Minerba Betancourt and Deborah Harris for their attentive feedback; to Daniel Rutherbories, for his patient help with the

framework and for solving more problems than I can count; to Andrew Olivier, whose explanations made many complex details more transparent; and to Mateus Carneiro, who offered early instruction and support. I owe much to this community for its openness and willingness to teach.

Among my fellow students at Tufts, I would like to mention Enrico D. Schiappacasse and Hyungsuk Son, who became close friends and whose companionship and example have remained a valued part of this journey.

I also wish to thank Gayle Grant, whose care and attention have made the Department of Physics and Astronomy at Tufts not only an efficient institution but also a kind and welcoming place.

My path in physics began in Kharkov, under the guidance of remarkable teachers. Sergey A. Lifits and Ilya M. Gelfgat first revealed to me the beauty of mathematics and physics. At V. N. Karazin Kharkov National University, I had the privilege of learning from many dedicated professors, but I am especially indebted to Prof. Igor A. Girka and Prof. Igor A. Berezhnoy, with whom I had the good fortune of many conversations and extended collaboration. Their commitment, encouragement, and humanity profoundly influenced my education and helped shape my understanding of physics as both a discipline and a vocation.

While an undergraduate student, I was fortunate to take part in the PARTI Internship Program at Fermilab. There, under the guidance of Tanaji Sen and Francois Ostiguy, I was introduced to the spirit of research in the United States. Their mentorship and example, and especially my many conversations with Francois, left a lasting impression on me and strengthened my resolve to pursue graduate studies abroad.

To my parents, I owe more than words can express. My Mother's energy and dedication shaped my education and taught me the value of persistence; my Father's curiosity and craftsmanship instilled in me the belief that understanding and skill are within reach of anyone willing to learn. I am also grateful to my sister, Tanya, for her affection, support, and encouragement, which have meant more than she may realize.

To my grandparents, I owe gratitude of a quieter kind. My grandfathers Boris and Stepan, who valued knowledge and encouraged my studies from an early age, and my grandmothers Nadya and Maria, whose love and care have always been a steady source of warmth and support, each contributed in their own way to the path that brought me here.

My deepest thanks belong to my beloved wife, Janina, for her patience, understanding, and unwavering support. Her presence has given meaning to every effort that went into this work, and her faith in me has sustained it through many stages. To our sons, Arkadii and Leonid, whose laughter and curiosity bring daily reminders of what is truly important, I dedicate this work with love and hope.

Funding Acknowledgment

The research presented in this dissertation was carried out within the MINERvA Collaboration, using the resources of the Fermi National Accelerator Laboratory (Fermilab), a U.S. Department of Energy, Office of Science, Office of High Energy Physics user facility. Fermilab is managed by FermiForward Discovery Group, LLC under Contract No. 89243024CSC000002. This work was supported in part by the U.S. Department of Energy under Grant DE-SC0019032 and by the Fermilab NPC Fellowship.

Sciences nourish the young,
Give joy to the old,
Adorn our lives in prosperity,
Shelter us in adversity;
Comfort in domestic labors,
No burden in distant travels.

Sciences serve everywhere:
Among nations and in solitude,
Amid city clamor and in silence,
Sweet in rest, pleasing in toil.

M. V. Lomonosov, 1747

1 Introduction

1.1 Background and Motivation

All human experience – sights, sounds, biology, and chemistry – is composed of a relatively small number of particles. Photons constitute the visible light, while electrons, protons, and neutrons build up the matter around us. However, beyond the limits of everyday experience — in the interiors of stars, in high-energy accelerators, and at minuscule timescales — there exists a diverse

spectrum of particles not commonly encountered in daily life. Among these elusive particles are neutrinos.

Neutrinos are among the most abundant particles in the universe, second only to photons. Produced abundantly in nuclear processes within stars and during cosmic events, neutrinos possess a unique characteristic: they interact extremely weakly with matter. Despite about 65 billion neutrinos passing through every square centimeter of your body each second, throughout an entire human lifetime, on average, only one neutrino interaction might occur within the human body.

Due to their elusive nature, neutrinos are studied with detectors of enormous size, located deep underground or embedded in polar ice, providing shielding against background radiation. Such experiments illustrate the complexity of neutrino detection—stopping a neutrino reliably would require about one light-year thickness of solid lead.

The theoretical framework that successfully explains the interactions and particles observed so far is the Standard Model (SM) of particle physics. While this model accurately describes an extensive range of phenomena from terrestrial to cosmic scales, it remains incomplete. The SM does not address critical questions about gravity, dark matter, dark energy, or the observed dominance of matter over antimatter in the universe.

One significant shortcoming of the original SM formulation was the assumption that neutrinos are massless particles. Experimental evidence, notably the phenomenon of neutrino oscillations—where neutrinos change types (or flavors) as they propagate—has demonstrated that neutrinos indeed have mass. This discovery necessitated extensions to the Standard Model, deepening our understanding of particle physics and opening doors to new physics beyond current theories.

Neutrino oscillations imply profound consequences. They hint at new physics and offer potential insights into fundamental puzzles, such as the matter-antimatter asymmetry of the universe. Addressing these mysteries has become a global research effort [18,1,2,7]. Accelerator-based neutrino experiments, for instance, send intense neutrino beams through Earth from near to far detectors

to measure neutrino oscillation probabilities. Accurate interpretation of these oscillation measurements depends critically on understanding neutrino interactions and precise modeling of both neutrino fluxes and interaction cross-sections.

This thesis addresses a specific aspect of neutrino interaction physics, focusing on charged-current neutrino interactions producing exactly two protons and no pions in the final state, detected in the MINERνA experiment exposed to the NuMI medium-energy neutrino beam. The chosen event topology—characterized by one lepton and two protons—probes processes such as two-particle-two-hole (2p2h) interactions and pion absorption phenomena, both of which remain poorly understood.

We present single-differential cross-section measurements for events containing exactly two protons in the final state. The measurements are made as a function of several critical kinematic observables: the cosine of the angle between the two most energetic protons, the leading proton momentum, and the subleading proton momentum. These observables provide unique sensitivity to nuclear effects, helping to advance theoretical modeling and contributing valuable data for future neutrino oscillation experiments, such as the Deep Underground Neutrino Experiment (DUNE)[7].

The structure of this thesis is as follows: rest of Chapter 1 provides theoretical background and motivation, including the current state of neutrino interaction physics and neutrino oscillations. Chapters 2 and 3 detail the experimental setup and the reconstruction methods used in MINERνA. Chapter 4 presents the measurement end-to-end: event selection, background tuning, unfolding, efficiency and flux corrections, systematic-uncertainty evaluation, and the resulting differential cross sections. Chapter 5 then summarizes the main findings and implications for neutrino physics.

1.2 The Standard Model

The Standard Model (SM) of particle physics is a well-established theoretical framework describing the fundamental particles that constitute matter and the interactions between them. Developed throughout the 20th century, the SM successfully explains a vast array of experimental results, making it one of the most tested and reliable theories in modern physics.

According to the Standard Model, all known matter is composed of fundamental particles called fermions, which possess half-integer spin and follow the Pauli exclusion principle. Fermions are divided into two main categories: quarks and leptons.

Quarks are the building blocks of protons and neutrons and carry fractional electric charges of either $+\frac{2}{3}$ or $-\frac{1}{3}$ of the elementary charge. They come in six "flavors": up (u), down (d), charm (c), strange (s), top (t), and bottom (b). Quarks are never found isolated in nature due to a property known as confinement; instead, they form composite particles called hadrons, such as protons (uud) and neutrons (udd).

Leptons, the other type of fermion, include the electron (e), muon (μ), tau (τ), and their corresponding neutrinos (ν_e, ν_μ, ν_τ). Unlike quarks, leptons do not participate in strong interactions.

Interactions between these fundamental particles are mediated by force-carrying particles called gauge bosons, which have integer spins. There are four primary gauge bosons:

- The photon (γ), mediating the electromagnetic force, which is responsible for electricity, magnetism, and light.
- The W and Z bosons ($W^{\pm}$, Z^0), which mediate the weak force responsible for radioactive decay and neutrino interactions.
- The gluon (g), mediating the strong force that holds quarks together inside protons and neutrons.

A special particle, the Higgs boson (H), was predicted by the Standard Model to explain how particles acquire mass through interactions with the Higgs field. Its discovery at the Large Hadron Collider (LHC) in 2012 confirmed a crucial component of the Standard Model.

Figure 1.1 summarizes the fundamental particles and forces described by the Standard Model.

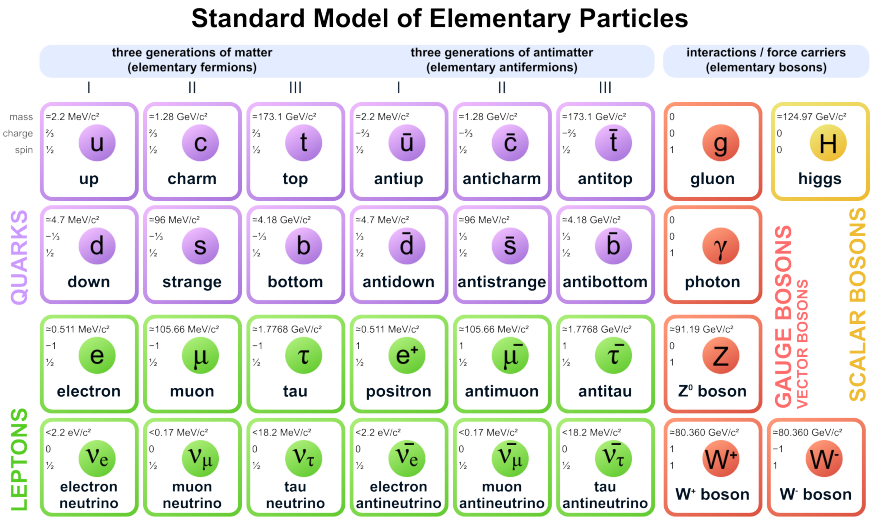

Figure 1.1: A visual representation of the fundamental particles and forces in the Standard Model. Figure from [25].

Despite its successes, the Standard Model has known limitations. It does not include a description of gravity, nor can it fully explain dark matter, dark energy, or the observed matter-antimatter asymmetry in the universe. These unresolved questions motivate ongoing experimental and theoretical research, aiming to explore phenomena beyond the Standard Model.

1.3 Neutrino Oscillations

One of the most fascinating discoveries in modern particle physics has been the phenomenon of neutrino oscillations. Originally proposed theoretically by Bruno Pontecorvo and further developed by Ziro Maki, Masami Nakagawa, and Shoichi Sakata, neutrino oscillation is the process by

which neutrinos can change their flavor states (ν_e, ν_μ, ν_τ) as they propagate through space. This phenomenon provides definitive evidence that neutrinos have non-zero masses, which is one of the few observations not predicted by the original formulation of the Standard Model.

1.3.1 Historical Context

Initially, neutrinos were considered massless particles within the SM framework. However, experimental results over the last several decades revealed significant discrepancies with this assumption. The first hints of neutrino oscillations came from solar neutrino experiments, notably the Homestake experiment[23], which detected significantly fewer electron neutrinos from the Sun than theoretically expected.

The decisive evidence emerged in 1998 from the Super-Kamiokande experiment[36], which studied atmospheric neutrinos produced when cosmic rays interact with the Earth's atmosphere. The experiment observed a clear deficit of muon neutrinos (ν_μ) traveling long distances through the Earth compared to those traveling shorter distances, conclusively demonstrating neutrino oscillations. This groundbreaking discovery was recognized with the 2015 Nobel Prize in Physics.

1.3.2 Neutrino Oscillation Formalism

Neutrino oscillations arise because neutrinos exist in quantum states of definite mass (mass eigenstates), labeled as ν_1, ν_2, and ν_3, which differ from their flavor eigenstates (ν_e, ν_μ, ν_τ). The relationship between the flavor eigenstates and mass eigenstates is described by the Pontecorvo–Maki–Nakagawa–Sakata (PMNS) matrix, a unitary matrix U:

$$\begin{pmatrix} \nu_e \\ \nu_\mu \\ \nu_\tau \end{pmatrix} = \begin{pmatrix} U_{e1} & U_{e2} & U_{e3} \\ U_{\mu 1} & U_{\mu 2} & U_{\mu 3} \\ U_{\tau 1} & U_{\tau 2} & U_{\tau 3} \end{pmatrix} \begin{pmatrix} \nu_1 \\ \nu_2 \\ \nu_3 \end{pmatrix} \tag{1.1}$$

The PMNS matrix can be parameterized as follows:

$$U = \begin{pmatrix} c_{12}c_{31} & s_{12}c_{13} & s_{13}e^{-i\delta_{CP}} \\ -s_{12}c_{23} - c_{12}s_{23}s_{13}e^{i\delta_{CP}} & c_{12}c_{23} - s_{12}s_{23}s_{13}e^{i\delta_{CP}} & c_{23}s_{13} \\ s_{12}s_{23} - c_{12}c_{23}s_{13}e^{i\delta_{CP}} & -s_{12}c_{23} - s_{12}c_{23}s_{13}e^{i\delta_{CP}} & c_{23}c_{13} \end{pmatrix} \tag{1.2}$$

where $s_{ij} = \sin\theta_{ij}$, $c_{ij} = \cos\theta_{ij}$, and δ_{CP} is the CP-violating phase, responsible for differences in the oscillation behaviors between neutrinos and antineutrinos.

The probability of a neutrino originally produced in flavor α being detected later in flavor β after traveling distance L (measured in km) is given by:

$$\begin{aligned} P(\nu_\alpha \to \nu_\beta) =& \delta_{\alpha\beta} - 4\sum_{j>k} \mathrm{Re}(U^*_{\alpha j}U_{\beta j}U_{\alpha k}U^*_{\beta k}) \sin^2\left(1.27\frac{\Delta m^2_{jk}L}{4E}\right) + \\ &+ 2\sum_{j>k} \mathrm{Im}(U^*_{\alpha j}U_{\beta j}U_{\alpha k}U^*_{\beta k}) \sin\left(2.54\frac{\Delta m^2_{jk}L}{2E}\right), \end{aligned}$$

where $\Delta m^2_{jk} = m^2_j - m^2_k$ are mass squared differences in eV^2/c^4, and E is the neutrino energy in GeV. Non-integer factors 1.27 and 2.54 appear because of omitted $c^3/\hbar$ and a conversion of units. The oscillation probability depends explicitly on neutrino energy and the distance traveled, highlighting the necessity of precise energy measurements and source-to-detector baselines in neutrino experiments.

1.3.3 Neutrino Oscillation Parameters

Oscillation experiments primarily measure the differences in squared masses of neutrino mass eigenstates, rather than their absolute masses.

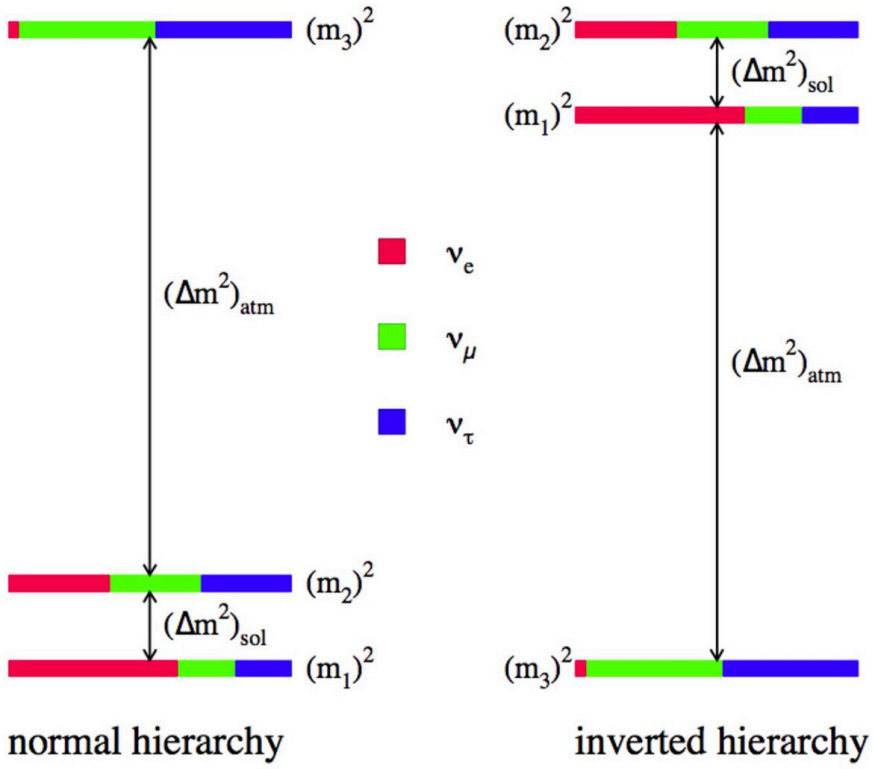

Figure 1.2: Visual illustration of two possible scenarios of neutrino mass hierarchy: normal and inverted. Figure from [22].

Currently known oscillation parameters from global fits are summarized in Table 1.1.

Table 1.1: Best-fit values for neutrino oscillation parameters as of 2024 [50].

Parameter	Value
Δm^2_{21}	$(7.53^{+0.18}_{-0.18}) \times 10^{-5}\ \mathrm{eV}^2$
Δm^2_{32} (Normal Hierarchy)	$(2.455^{+0.028}_{-0.028}) \times 10^{-3}\ \mathrm{eV}^2$
Δm^2_{32} (Inverted Hierarchy)	$(-2.529^{+0.029}_{-0.029}) \times 10^{-3}\ \mathrm{eV}^2$
$\sin^2\theta_{12}$	$0.307^{+0.013}_{-0.013}$
$\sin^2\theta_{23}$ (Normal Hierarchy)	$0.558^{+0.015}_{-0.021}$
$\sin^2\theta_{23}$ (Inverted Hierarchy)	$0.553^{+0.016}_{-0.024}$
$\sin^2\theta_{13}$	$0.021^{+0.0007}_{-0.0007}$
δ_{CP}/π	$1.19^{+0.22}_{-0.22}$

1.3.4 Long-Baseline Neutrino Oscillation Experiments

Current and future neutrino oscillation experiments, such as T2K, NOνA, and DUNE, aim to determine the neutrino mass hierarchy (the ordering of neutrino mass eigenstates), precisely measure the CP-violating phase δ_{CP}, and resolve the octant ambiguity of θ_{23}. These experiments use intense, accelerator-produced neutrino beams and measure oscillation probabilities by comparing neutrino interaction rates at near and far detectors placed at varying distances.

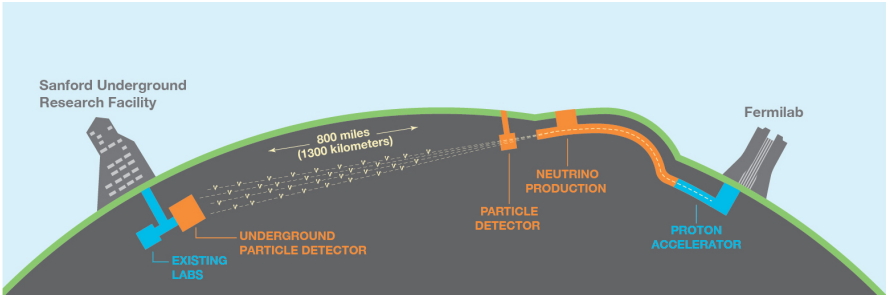

Figure 1.3: Scheme of the Deep Underground Neutrino Experiment (DUNE) — prospective long-baseline neutrino experiment[8].

Figure 1.4 shows recent data from the NOvA experiment[4]. The left panel shows unoscillated data as collected by the Near Detector, and the right two panels, for ν_μ and ν_e CC interactions in the Far Detector, show evidence of oscillations through the disappearance of muon neutrinos (middle panel) and the appearance of electron neutrinos (right panel).

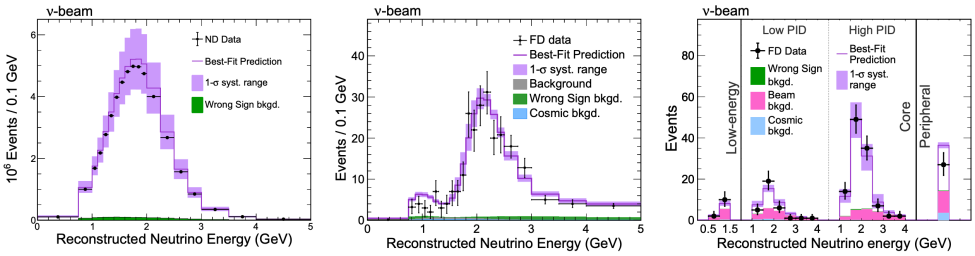

Figure 1.4: Neutrino energy spectra from the NOvA experiment: ν_μ CC events in the Near Detector (left), ν_μ CC events in the Far Detector (middle), and ν_e CC events in the Far Detector for four different (right).[4].

1.3.5 Relevance to Neutrino Interaction Studies

Accurate measurements of neutrino oscillation parameters critically depend on precise understanding and modeling of neutrino interactions with nuclei. Since detectors measure neutrino flavor indirectly through interaction products, uncertainties in neutrino-nucleus interaction cross sections can significantly bias oscillation parameter extraction. This necessitates detailed study and measurement of neutrino cross sections and nuclear effects, forming the core motivation of this thesis.

Thus, comprehensive characterization of neutrino interactions, particularly in complex nuclear environments, is an essential component of the experimental neutrino physics program aimed at unveiling fundamental neutrino properties.

1.4 Charged Current Neutrino-Nucleus Interactions

Neutrino interactions with atomic nuclei form the cornerstone of accelerator-based neutrino experiments. Precise measurements of these interactions are essential for accurate interpretation of neutrino oscillation data and thus for answering fundamental questions about neutrino properties and the structure of the Standard Model itself. Among the various types of neutrino-nucleus interactions, Charged Current (CC) interactions play a central role due to their distinct experimental signatures.

In CC interactions, an incoming neutrino interacts with a nucleon within the nucleus via the exchange of a charged W-boson. This interaction changes the neutrino into its corresponding charged lepton partner (e.g., a muon neutrino transforms into a muon). The presence of the charged lepton in the final state provides a clear experimental signature, facilitating event reconstruction and classification.

However, interpreting CC neutrino-nucleus interactions is complicated by the nuclear environment. Nuclei are complex, dense systems of strongly interacting nucleons, and this internal com-

plexity significantly affects how neutrino interactions occur and how resulting particles propagate. Various phenomena such as nuclear binding energies, nucleon momentum distributions, multi-nucleon correlations, resonance excitation, and final state interactions (FSIs) modify the observed outcomes of neutrino interactions. These nuclear effects need to be carefully understood and modeled to reduce systematic uncertainties in neutrino experiments.

In the following subsections, we discuss in detail the primary categories of CC neutrino-nucleus interactions relevant to accelerator neutrino experiments:

- **Quasi-Elastic (QE) and Deep Inelastic Scattering (DIS)**: Interactions characterized by low (QE) and high (DIS) hadronic energy transfer, respectively, and their importance in event reconstruction.
- **Resonance Pion Production**: Neutrino interactions exciting nucleons into resonance states, resulting in pion emission.
- **Coherent Pion Production**: Interactions in which neutrinos produce pions without altering the nucleus, resulting in distinct event topologies.
- **Modifications to Nuclear Medium**: Including the Relativistic Fermi Gas (RFG) model and multi-nucleon correlations (Random Phase Approximation (RPA) and two-particle two-hole (2p2h) processes), capturing nuclear dynamics that alter neutrino interaction signatures.
- **Nuclear Final State Interactions (FSI)**: Processes that particles undergo within the nuclear medium after the initial neutrino interaction, significantly complicating the reconstruction of interaction dynamics.

An understanding of each of these components is crucial, since each type of interaction, each nuclear modification, and each FSI mechanism introduces unique challenges and uncertainties that

must be properly addressed. The brief analysis of CC neutrino-nucleus interactions, introduced in this chapter, provides the theoretical background and the experimental context.

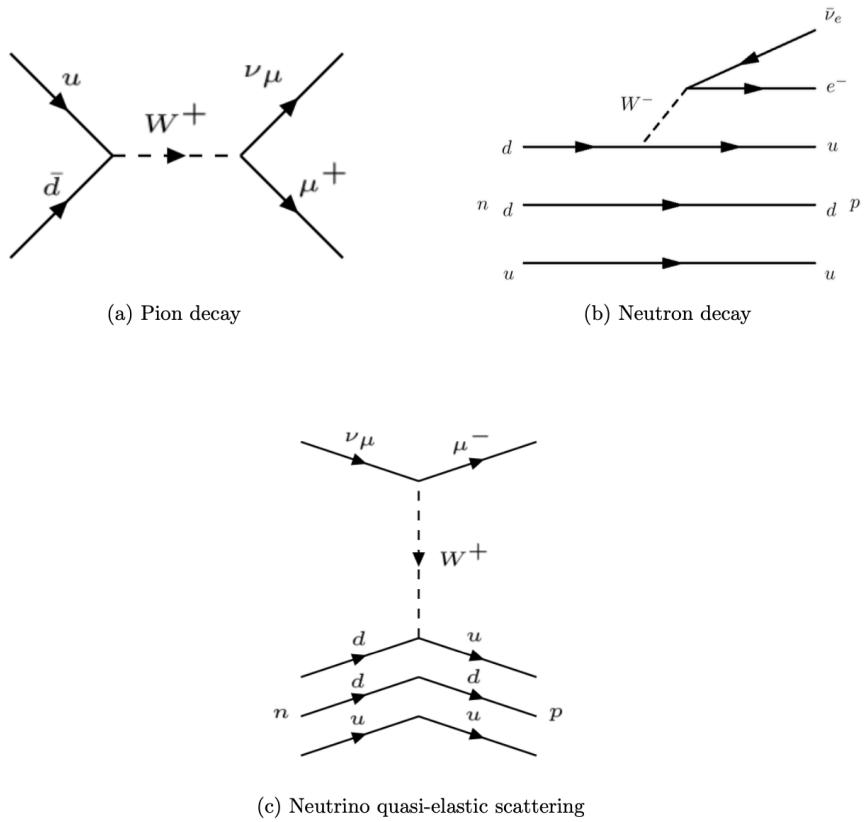

(a) Pion decay

(b) Neutron decay

(c) Neutrino quasi-elastic scattering

Figure 1.5: Feynman diagrams illustrating several charged–current weak processes: (a) charged pion decay, (b) neutron beta decay, and (c) neutrino–nucleon quasielastic scattering. Adapted from[47].

1.4.1 Quasi-Elastic (QE) and Deep Inelastic Scattering (DIS)

Quasi-Elastic (QE) neutrino scattering off a nucleon is a fundamental process characterized by relatively low momentum transfer. In these interactions, the incoming neutrino transforms into its corresponding charged lepton, and the outgoing hadronic system consists of a single nucleon consistent with charge conservation. Due to the simplicity of the QE process, neutrino energies can be reconstructed relatively accurately using only the final-state lepton kinematics. However, precise

modeling must carefully account for nuclear effects such as nucleon binding energies, momentum distributions, and final state interactions (FSI)[20,44].

The theoretical description of QE neutrino scattering is given by the Llewellyn–Smith formalism[42]. A key component of this formalism is the axial-vector form factor $G_A(Q^2)$, typically parametrized as:

$$G_A(Q^2) = \frac{g_A}{\left(1 + \frac{Q^2}{m_A^2}\right)^2}, \tag{1.3}$$

where $g_A \approx 1.27$ is the axial coupling constant and m_A is the axial mass parameter, determined experimentally and typically around 1 GeV/c^2 [43]. Precise measurement of m_A is essential for accurate neutrino cross-section modeling, directly impacting neutrino oscillation analyses[46]. Alternative parametrizations provide more flexibility to describe the Q^2 dependence, and the calculation of the axial form factor using lattice QCD is an area of active research[49].

In contrast, Deep Inelastic Scattering (DIS) occurs at higher energies with substantial energy transfer to the hadronic system. During DIS, neutrinos scatter off individual quarks within nucleons, resulting in nucleon fragmentation and the production of multiple hadrons. DIS processes, characterized by large invariant masses of the final-state hadronic system, provide valuable insights into the nucleon's partonic (quark and gluon) structure[30,64]. However, accurate neutrino energy reconstruction from DIS events remains challenging due to the complexity and multiplicity of final-state hadrons.

Both QE and DIS processes are actively studied, as precise modeling of these interactions significantly enhances the interpretation of experimental neutrino data[33,32,48].

1.4.2 Resonance Pion Production

In resonance pion production, a neutrino interaction excites the struck nucleon to a higher-energy resonance state. These resonance states are unstable, rapidly decaying into nucleons accompanied

by mesons, most commonly pions. The resonance production mechanism dominates neutrino interactions at energies between the quasi-elastic (QE) and deep inelastic scattering (DIS) regimes, roughly in the invariant hadronic mass region 1.2 GeV $\lesssim W \lesssim$ 1.8 GeV.

The interaction proceeds primarily through the charged-current (CC) channel, as described in the following example:

$$\nu_\ell + N \to \ell^- + \Delta^{++,+,0,-}, \tag{1.4}$$

where Δ represents a spin $3/2$ baryon resonance excited by the neutrino interaction, ν_ℓ is the incoming neutrino, N is the target nucleon, and ℓ^- is the outgoing charged lepton.

The resonance baryon subsequently decays predominantly via:

$$\Delta \to N' + \pi, \tag{1.5}$$

resulting in an observable final state of a charged lepton, nucleon, and pion.

Experimentally, resonance pion production is highly relevant because the produced pions significantly affect the energy reconstruction of neutrino events and hence the measurement of neutrino oscillation parameters.

The most widely used theoretical model for resonance production in neutrino event generators is the Rein-Sehgal (RS) model[55]. The RS model is based on a relativistic quark model and includes contributions from 18 resonances with invariant masses $W < 2.0$ GeV. The original RS model formulation includes interference between resonances that share identical spin and orbital angular momentum. However, implementations of the RS model vary among neutrino event generators. For example, the GENIE 2.X series, which the present simulation is based on, does not incorporate such interference terms. Thus, while the common final state $\mu^- n \pi^+$ receives contributions primarily from resonances such as $\Delta(1232)$, $\Delta(1920)$, and $N(1720)$, these contributions are combined incoherently in GENIE 2.X.

Direct non-resonant contributions (non-resonant inelastic processes) can also lead to pion production and complicate resonance production modeling. To achieve improved agreement with experimental data, the Rein-Sehgal model includes an incoherently added non-resonant isospin-1/2 contribution. However, this treatment does not accurately capture interference effects between resonant and non-resonant contributions, potentially shifting the apparent resonance peak positions.

Modern neutrino interaction event generators using the RS model for resonance production must carefully avoid double-counting, particularly in transition regions where DIS contributions become relevant. Standard DIS hadronization models do not perform well at lower invariant mass regions (below $W \approx 2$ GeV), emphasizing the importance of robust resonance modeling.

Recent extensions to the original RS model, such as the work by Kabirnezhad[39], aim to explicitly incorporate interference effects between resonant and non-resonant terms, potentially providing more accurate modeling of resonance pion production processes. Experimental tests of these advanced theoretical frameworks remain a priority for contemporary neutrino scattering experiments.

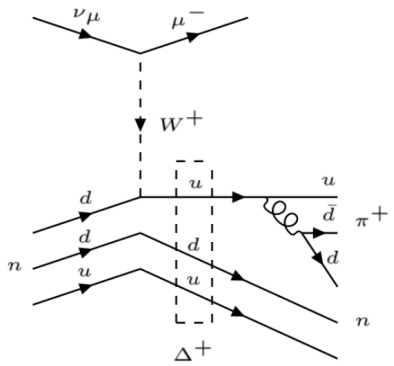

Figure 1.6: Feynman diagram showing charged–current neutrino–nucleon scattering proceeding via Δ^+ resonance excitation and subsequent pion emission. The Δ^+ can decay into either $n\pi^+$ or $p\pi^0$ final states, while the analogous reaction on a proton yields a π^+ and a p. Adapted from[47].

1.4.3 Modifications due to the Nuclear Medium

In neutrino-nucleus interactions, the internal nuclear environment plays a crucial role in modifying the initial neutrino-nucleon interaction. These nuclear effects significantly affect the observed kinematics and final state particle content, thus complicating experimental interpretations. An accurate representation of these nuclear medium modifications is essential for interpreting neutrino experimental results and for precise neutrino oscillation measurements.

Relativistic Fermi Gas Model

A common theoretical model to describe the initial state nucleon within the nuclear medium is the Relativistic Fermi Gas (RFG) model, introduced by Smith and Moniz[59]. In this model, nucleons are treated as quasi-free particles confined within a nuclear potential well, characterized by a uniform distribution of nucleon momentum up to a maximum Fermi momentum $k_F \approx 250\ \mathrm{MeV}/c$. Additionally, a constant nuclear binding energy (approximately 30 MeV) is assumed.

While the RFG model provides a convenient baseline, it is known to oversimplify nuclear dynamics, particularly missing important details such as short-range nucleon correlations and nuclear structure effects. Therefore, more sophisticated models, including local Fermi gas[51] and spectral function approaches[20], have been developed to better match experimental observations. A spectral function describes the probability of finding a nucleon within the nucleus with a given momentum and removal energy, thus providing a more realistic representation of nuclear structure and correlations.

Multi-Nucleon Correlations: npnh Processes

Neutrino interactions can also involve correlated nucleon pairs or groups, leading to so-called multi-nucleon knockout processes or npnh (n-particle n-hole) interactions. These interactions occur

when a neutrino interacts with nucleons correlated within the nucleus, causing the simultaneous ejection of multiple nucleons and leaving multiple *holes* in the nuclear medium.

The simplest type of npnh interaction is the one-particle one-hole (1p1h) interaction. In a 1p1h interaction, the neutrino interacts primarily with a single nucleon, knocking it out of the nuclear medium and leaving one hole behind. Such interactions typically correspond to quasi-elastic (QE) events and form the simplest and most commonly studied neutrino-nucleus interactions.

However, more complex multi-nucleon processes can also occur, notably the two-particle two-hole (2p2h) interactions. In 2p2h interactions, the neutrino interacts simultaneously with a correlated nucleon pair, typically a proton–neutron (pn) pair[44,51]. This interaction leads to the emission of two nucleons and the creation of two holes within the nucleus, significantly affecting reconstructed event kinematics. The presence of 2p2h interactions can substantially increase measured cross-sections in the quasi-elastic region and in the kinematic "dip" between the quasi-elastic and resonance production regions[51].

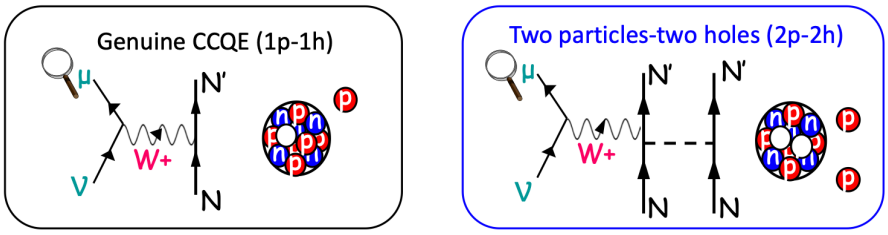

Figure 1.7: Illustration of nuclear multi-nucleon correlations (npnh processes). Shown are examples of 1p1h (left) and (b) 2p2h (right) interactions. Adapted from[40].

2p2h processes can be explained theoretically using meson-exchange current (MEC) models, in which correlated nucleon pairs interact through the exchange of virtual mesons (primarily pions). MEC diagrams involve multiple interaction vertices and significantly increase interaction rates at low to moderate momentum transfers (Q^2)[51,44].

Random Phase Approximation (RPA)

An additional nuclear effect arises from the collective behavior of nucleons within the nuclear medium, described by the Random Phase Approximation (RPA). The RPA formalism attempts to incorporate the long-range correlations and polarization effects within the nucleus. When included in neutrino-nucleus interaction models, RPA corrections generally reduce the interaction rates at low momentum transfers, reflecting suppression due to coherent nuclear responses.

The combined effect of RPA corrections and npnh processes results in a complex interplay. The RPA tends to suppress event rates at lower momentum transfers, while npnh (especially 2p2h) interactions increase these rates, requiring careful modeling and interpretation in neutrino experiments.

Accurately modeling these nuclear medium modifications is critical for reducing uncertainties and achieving the precision needed for neutrino physics research, especially for neutrino oscillation experiments.

1.4.4 Nuclear Final State Interactions (FSI)

After the initial neutrino interaction within the nucleus, the produced particles must propagate through the dense nuclear medium. During this propagation, these particles can undergo further interactions — known collectively as Final State Interactions (FSIs) — which significantly alter the observed event topologies and complicate event reconstruction. Understanding FSIs is crucial for correctly interpreting neutrino-nucleus interactions and accurately extracting underlying neutrino interaction physics from experimental data.

The key processes involved in FSIs include:

- **Elastic scattering**: Produced hadrons scatter elastically off nucleons within the nucleus, resulting in changes to their trajectories without altering their identities.

- **Inelastic scattering**: Hadrons lose energy or excite nucleons through inelastic collisions, producing secondary particles or resonances.
- **Charge exchange reactions**: Hadrons can exchange charge with nucleons (e.g., a charged pion converting to a neutral pion or vice versa).
- **Absorption**: Produced particles (especially pions) may be absorbed by nucleon pairs or clusters within the nucleus, leading to their disappearance from the final state.
- **Particle emission and secondary production**: Secondary particles can be emitted as a consequence of interactions, increasing multiplicities and complicating event signatures.

These FSI processes introduce significant complexity. For instance, a neutrino-induced pion might be absorbed, resulting in a final state indistinguishable from a quasi-elastic-like interaction. Similarly, elastic or inelastic scattering of outgoing nucleons can distort energy reconstruction and angular distributions, challenging the precise measurement of neutrino energy.

Accurate modeling of FSIs is a non-trivial challenge due to the complexity of nuclear dynamics. Theoretical descriptions generally rely on approaches such as intranuclear cascade models, in which particles are propagated step-by-step through the nucleus, using interaction probabilities informed by empirical hadron-nucleus scattering data and nuclear theory calculations[28].

Modern neutrino event generators, including GENIE, NEUT, and NuWro, implement sophisticated FSI models based on these cascade approaches, often calibrated against experimental data from pion- and proton-nucleus scattering experiments. However, considerable uncertainties remain, underscoring the importance of dedicated measurements of FSIs and continuous refinement of theoretical models.

The precise treatment of FSIs remains essential for neutrino physics, particularly in precision neutrino oscillation experiments, where accurate event reconstruction is critical. Further experimental and theoretical advancements in our understanding of nuclear FSIs will continue to play a

significant role in refining neutrino interaction models and in the accurate interpretation of neutrino experiment results.

1.5 Previous Measurements

Understanding neutrino-nucleus interactions and their associated cross sections is critical to current and future neutrino oscillation experiments. Charged-current (CC) interactions involving two protons and no pions (CC2p0π) in the final state provide a particularly valuable window into multi-nucleon correlations and nuclear medium effects, such as two-particle two-hole (2p2h) processes. However, until recently, measurements specifically targeting these final states were scarce, and comprehensive experimental data remains limited.

An early significant effort to measure neutrino-argon interactions came from the ArgoNeuT collaboration [6], utilizing the NuMI antineutrino beam at Fermilab. ArgoNeuT measured inclusive muon neutrino and antineutrino CC differential cross sections on argon, providing critical early data that demonstrated the feasibility of detailed cross-section measurements in liquid argon time projection chambers (LArTPCs). Although this measurement did not specifically focus on CC2p0π events, the reported inclusive data set a foundation for understanding neutrino-argon interactions and paved the way for more exclusive measurements.

A major step toward explicitly measuring CC interactions with exactly two protons in the final state was accomplished by the MicroBooNE collaboration [3]. Using a LArTPC detector in the Booster Neutrino Beamline at Fermilab, MicroBooNE provided the first measurement of differential cross sections for muon neutrino CC interactions on argon with precisely two protons and no pions in the final state. This analysis explicitly targeted multi-nucleon correlation events, offering a direct experimental handle on npnh interactions, particularly the 2p2h processes. The results from MicroBooNE provided critical benchmarks for theoretical neutrino interaction models and

highlighted the significance of detailed nuclear modeling in interpreting neutrino data.

Prior experimental efforts have established foundational knowledge and valuable experimental benchmarks for neutrino-argon interactions, with the most recent MicroBooNE measurements explicitly addressing the CC2p0π final state. These measurements have significantly informed neutrino interaction modeling and provided necessary context for more specialized analyses, such as the one described in this thesis.

If I have seen further, it is by standing on the shoulders of giants.

Isaac Newton

2

MINERvA Experiment

2.1 NuMI Beam

The Neutrinos at the Main Injector (NuMI) beamline at Fermilab was specifically designed to produce a high-intensity muon neutrino (ν_μ) beam, with the ability to adjust the neutrino energy spectrum and to produce either neutrinos or antineutrinos. MINERvA used NuMI to study neutrino–nucleus interactions with fine granularity, while long-baseline oscillation experiments such as MI-

NOS and NOvA exploited the same beam for precision oscillation measurements [11,9].

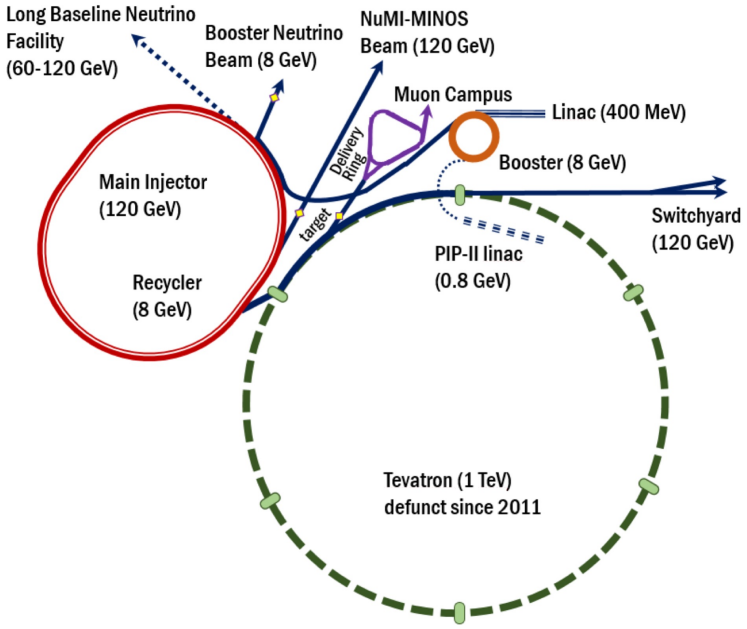

Figure 2.1: The Fermilab accelerator complex, including the 400 MeV linac, 8 GeV Booster, 120 GeV Main Injector, and associated beamlines. The NuMI beamline, used by MINERvA, receives protons from this chain. Future facilities (dashed lines) include PIP-II and the LBNF beamline. Figure adapted from [58].

The beam is created in four steps. First, protons with energy 120 GeV are extracted from the Main Injector and steered onto a graphite target. Second, that collision produces many short-lived charged mesons, mainly pions ($\pi^{\pm}$) and kaons ($K^{\pm}$). Third, a pair of pulsed magnetic horns focuses mesons of one electric charge into the forward direction; flipping the horn polarity selects the opposite charge. Because positively charged mesons decay to neutrinos and negatively charged mesons decay to antineutrinos, this focusing step determines whether the beam is predominantly ν_μ or $\bar{\nu}_\mu$. Finally, the focused mesons fly down a decay pipe approximately 675 m in length where they decay via weak processes such as

$$\pi^+ \to \mu^+ + \nu_\mu, \quad \pi^- \to \mu^- + \bar{\nu}_\mu$$

and

$$K^+ \to \mu^+ + \nu_\mu, \quad K^- \to \mu^- + \bar{\nu}_\mu.$$

Muons and remaining undecayed hadrons were stopped by an absorber composed of steel and concrete at the end of the decay pipe, while neutrinos continued through unimpeded, forming the final neutrino beam.

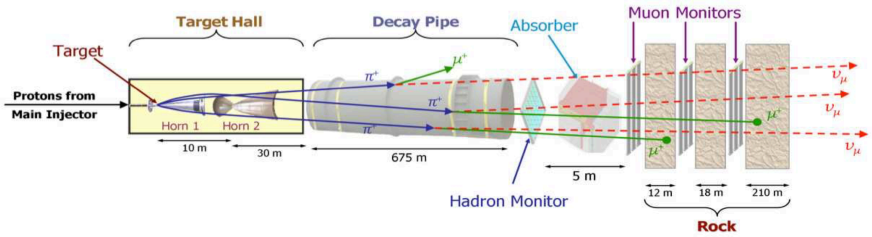

Figure 2.2: Schematic overview[10] of the NuMI beamline at Fermilab.

The energy profile and flux composition of the NuMI neutrino beam depended significantly on the beamline configuration, including horn currents and target positions. During the MINERvA experiment's run period, the NuMI beam operated primarily in the medium-energy mode, yielding neutrino energies predominantly in the 2–10 GeV range. This energy range was optimized for studying neutrino interactions and neutrino oscillations relevant to experiments like NOvA.

The MINERvA experiment concluded data collection in 2019, although the NuMI beamline continues to operate, providing neutrino beams for the ongoing NOvA experiment, prototype DUNE detectors, and prototyping for other future neutrino research and applications planned at Fermilab.

MINERvA accumulated substantial integrated exposures in both the earlier *low-energy (LE)* and the later *ME* running:

- **LE running (2009–2012):** about 4.0×10^{20} POT in FHC (ν_μ–enhanced) and 1.7×10^{20} POT in RHC ($\bar{\nu}_\mu$–enhanced).

- **ME running (2013–2019):** approximately 1.2×10^{21} POT in *each* horn polarity (FHC and RHC).

Within this thesis, the analysis sample corresponds to the ME FHC exposure (see Chapter 4 for the exact POT used).

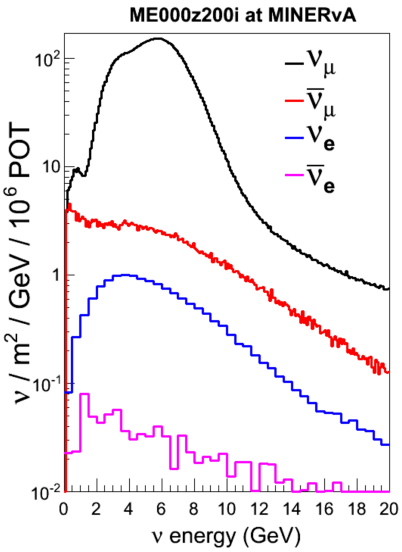

Figure 2.3: Neutrino flux spectrum[15] of the NuMI beam during MINERvA's medium-energy run period.

Figure 2.4 shows the total number of protons on target (POT) delivered to the NuMI medium energy beamline as a function of time. The data analyzed in this thesis are from the forward horn current (neutrino mode) running of the beamline. Also shown are the livetime of the MINERvA and MINOS detectors during beam operations, for a combined efficiency of 92.7%.

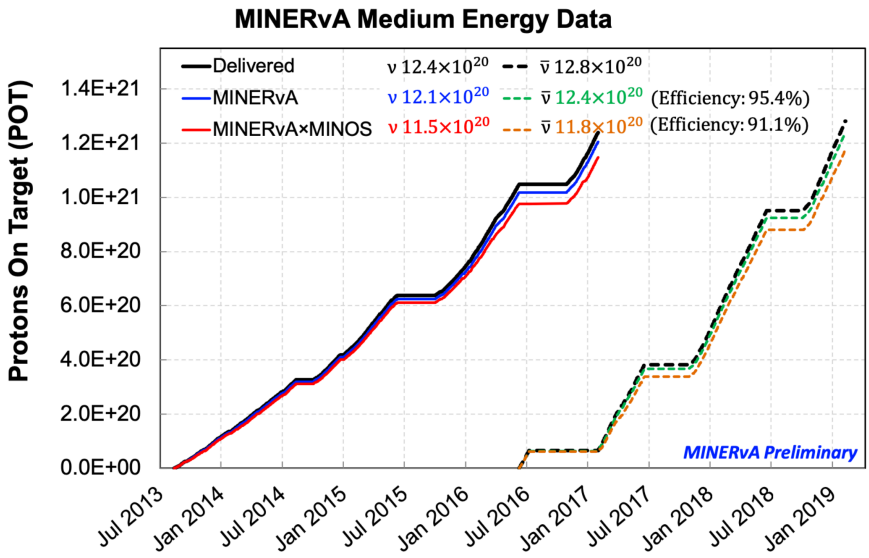

Figure 2.4: Total number of Protons on Target (POT) delivered to the NuMI beamline in medium energy configuration as a function of time.

2.2 MINERvA Detector

The MINERvA (Main Injector Experiment for ν-A) detector was specifically designed to perform precision measurements of neutrino interactions across a range of energies provided by the NuMI beamline at Fermilab. Its primary goal was to study neutrino-nucleus interactions with high granularity and excellent tracking capabilities, enabling detailed reconstruction of final-state particles produced in neutrino interactions.

The detector was positioned approximately 1 kilometer downstream from the NuMI target, located directly upstream of the MINOS Near Detector, which provided complementary muon energy and charge measurements. MINERvA collected data between 2009 and 2019, spanning both low-energy (LE) and medium-energy (ME) NuMI beam configurations.

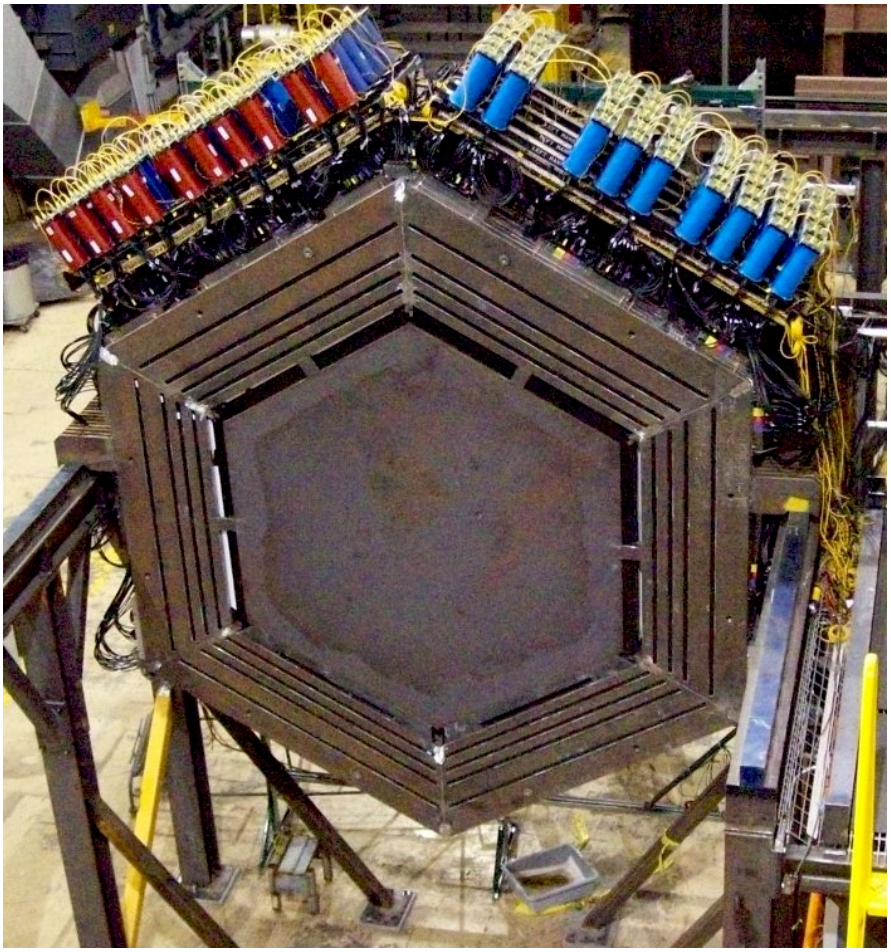

Figure 2.5: Photograph of the MINERvA detector in the NuMI beamline hall at Fermilab. Image adapted from Ref. [62].

2.2.1 Detector Design

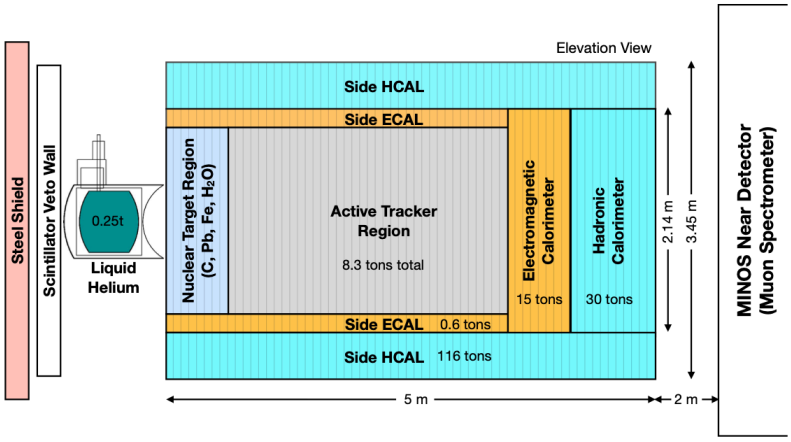

(a) MINERvA detector side view. The beam enters from the left.

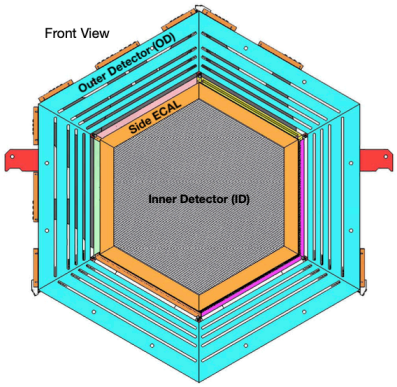

(b) MINERvA tracking plane front view.

Figure 2.6: Side and tracking plane views of MINERvA detector[47].

MINERvA was constructed as a fine-grained tracking calorimeter composed primarily of plastic scintillator modules interspersed with passive nuclear targets.

The active planes have a hexagonal outline, but the individual scintillator strips have a triangular

cross section and are assembled into planes oriented in three stereo views (X, U, V at $0°$, $+60°$, and $-60°$). This geometry provides precise 3D tracking and vertexing by combining the complementary views.

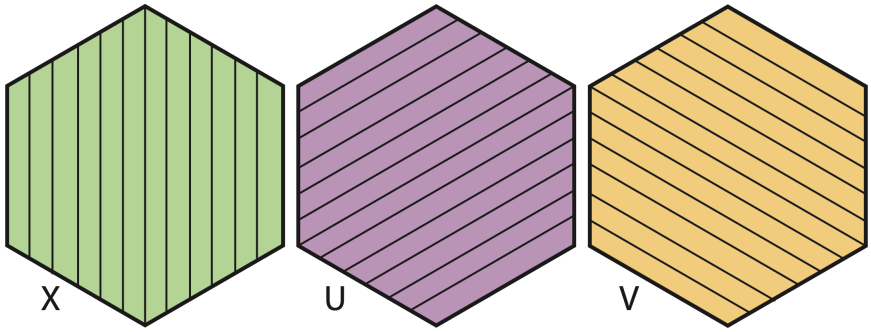

Figure 2.7: Diagram illustrating the three scintillator plane orientations (X, U, and V) used in MINERvA's active tracking region. This configuration provides three-dimensional reconstruction capability by combining hits from multiple views. Figure from Ref. [47].

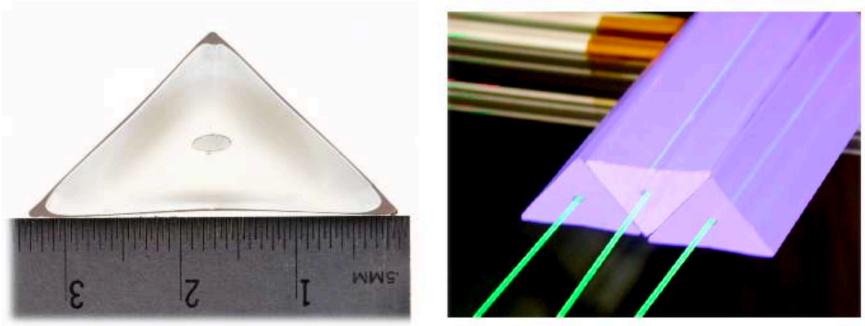

Figure 2.8: Schematic of the triangular scintillator strips and interleaved plane geometry used in the active tracking region of the MINERvA detector. This design provides fine spatial resolution for charged particle tracking. Figure adapted from Ref. [13].

The active material is co–extruded polystyrene scintillator. Each strip carries an external TiO_2 reflective layer (co–extruded) that improves light trapping, and a central, extruded hole into which a wavelength-shifting (WLS) fiber is *glued* (the fiber is not doped into the plastic). The WLS fiber absorbs blue scintillation photons and re-emits green light, which is transported along the fiber

with an attenuation length of order a few meters. The fiber is optically coupled via clear fiber to multi-anode photomultiplier tubes (PMTs). Attenuation and position-dependent response are corrected using per-strip calibration maps derived from through-going muons and dedicated light-injection data. The resulting light yield in the tracker is at the level of several photoelectrons per MeV at normal incidence (position dependent along the strip); quantitative performance metrics and stability versus time are documented in the MINERvA NIM paper [13].

The active region of MINERvA was segmented into the following regions:

- **Tracker Region:** The core of the detector, composed solely of plastic scintillator, provided high-resolution tracking of charged particles and precise vertex reconstruction. The typical hit position resolution was about 3 mm, with vertex resolution of 2–3 mm transversely and $\sim$5 mm longitudinally. Muon angular resolution was better than 9 mrad, and the momentum resolution for stopping protons measured by range was better than 5% [13]. The tracker region has been central to a broad range of MINERvA analyses, including charged-current quasi-elastic scattering [33] and proton kinematics studies [63].

- **Electromagnetic and Hadronic Calorimeters:** Downstream of the tracker, electromagnetic calorimeter (ECAL) modules alternated layers of scintillator and lead, providing enhanced photon and electron identification. The ECAL achieved an electron energy resolution of about 11.5% at 0.4–0.5 GeV in the EH (ECAL+HCAL, test-beam configuration) and 9.1% in TE (Tracker+ECAL), validated using the dedicated test-beam program [24]. Further downstream, hadronic calorimeter (HCAL) modules alternated scintillator with steel layers to contain and measure hadronic showers, with hadronic (recoil) energy resolution of $\sigma/E = 0.134 \oplus 0.290/\sqrt{E(\text{GeV})}$ [13]. These calorimeters were essential for analyses such as coherent pion production [37] and single-pion production cross sections [52].

- **Nuclear Target Region:** Positioned upstream of the tracker, this region included passive

targets composed of different nuclear materials (carbon, iron, lead, water, and helium) interleaved with tracking modules. This design enabled comparative measurements of neutrino interactions across different nuclear media while maintaining vertex resolution of a few millimeters for events in the target region, ensuring reliable association of interactions with the correct target material [13]. Analyses using this region include A-dependent cross-section ratios [31] and studies of nuclear effects in pion production [17].

2.2.2 Calibration and Monitoring

Ensuring high data quality and precision required meticulous calibration and continuous monitoring of the MINERvA detector. Calibration procedures corrected variations in scintillator response, PMT gains, and electronics over time. A key external constraint on the calorimetric response came from the dedicated MINERvA test-beam program, which exposed a small replica detector to charged hadrons and electrons to calibrate and validate the electromagnetic and hadronic energy scales and to tune the GEANT4-based simulation of shower development [13].

Key tasks. (i) Energy-scale calibration with cosmic-ray and neutrino-induced muons; (ii) time calibration for inter-module synchronization; (iii) PMT/electronics gain monitoring and corrections.

Stability. Time-dependent calibration constants tracked modest drifts (e.g., PMT gains) and occasional channel outages; stability was validated with throughgoing muons and periodic reprocessing [13].

Performance benchmarks. For hadronic recoil energy in CC interactions, the effective calorimetric resolution follows $\sigma/E = 0.134 \oplus 0.290/\sqrt{E(\mathrm{GeV})}$ [13]. In the electromagnetic sector, the test-beam program found electron energy resolutions of about 11.5% at $E = 400$–500 MeV in the full detector simulation and 9.1% in the replica detector [14].

It is the mark of an educated mind to rest satisfied with the degree of precision that the nature of the subject admits and not to seek exactness where only an approximation is possible.

Aristotle

3

Neutrino event reconstruction and simulations

3.1 Event Reconstruction

Event reconstruction algorithms processed raw data to identify neutrino interaction vertices and determine the kinematics of outgoing particles. The reconstruction pipeline involved several metic-

ulously executed steps:

- **Hit Reconstruction:** The initial step involved translating raw electronic signals from PMTs into individual ”hits”, representing localized energy deposits in scintillator strips. This step included corrections for PMT gain variations and electronics response to ensure accurate energy calibration.

- **Cluster Formation:** Within each scintillator view (X, U, or V), adjacent hits in neighboring strips and consistent in time were grouped into clusters, representing localized energy deposits likely originating from single particles. These two-dimensional clusters formed the basis for subsequent cross-plane matching and three-dimensional track building.

- **Track Reconstruction:** Clusters were combined to reconstruct particle tracks. Tracking algorithms utilized pattern recognition and trajectory fitting methods, including Kalman filters, to determine particle momenta and directions. Multiple Coulomb scattering and energy loss were systematically accounted for to enhance tracking precision [13].

- **Vertex Reconstruction:** Reconstructed tracks were extrapolated backward to determine a common interaction vertex. Vertex algorithms handled multiple-track interactions, employing iterative fitting procedures to optimize vertex position accuracy and resolve ambiguities.

- **MINOS Muon Matching:** Tracks exiting the downstream end of MINERvA were geometrically and temporally matched to tracks reconstructed in the MINOS Near Detector, located directly behind MINERvA. This procedure provided an extended muon lever arm, significantly improving momentum resolution via curvature in the magnetic field, and enabled charge identification. MINOS matching was therefore an essential ingredient in reliable muon reconstruction.

- **Particle Identification (PID):** Identification relied on distinguishing characteristics in energy deposition profiles, timing, and track topology. Muons were identified primarily through MINOS matching, while protons and pions were distinguished by their energy loss patterns (dE/dx), track curvature, and stopping behavior. Electrons and photons were identified via calorimetric showers in the ECAL region.

- **Energy Reconstruction:** Particle energies were reconstructed using calibrated measurements of deposited energy, correcting for detector response and containment. Hadronic and electromagnetic showers underwent tailored reconstruction methods to accurately measure shower energy and shape.

Rigorous validation of these reconstruction algorithms included systematic comparisons between data and Monte Carlo simulations. Iterative improvements were guided by performance metrics, including reconstruction efficiency, resolution, and systematic uncertainty minimization.

3.1.1 Hit Reconstruction

Data acquisition records integrated charge and timing for each readout channel within the beam spill window. Reconstruction begins with:

1. **Pedestal/gain corrections:** Channel-by-channel pedestals are subtracted and PMT gains applied to convert ADC counts to photoelectrons (PE).

2. **Light attenuation corrections:** Position-dependent corrections along each scintillator strip are applied (based on in situ through-going muons and bench measurements of the WLS fiber attenuation), yielding a uniform PE response versus longitudinal hit position. The attenuation length of the wavelength-shifting fibers is approximately $7-8$ m [13], consistent with the strip length, so the correction is essential for uniform response.

3. **PE → energy calibration:** A global PE-to-MeV factor anchored to minimum-ionizing muons establishes the absolute visible energy scale (with time-dependent monitoring), producing calibrated hit energies E_{hit} and associated times t_{hit}.

Hits are then grouped into *time slices* using nearest-neighbor logic in time (tight windows around the beam spill microstructure plus out-of-time cosmic veto windows). This suppresses pile-up and isolates single interaction candidates. The resulting time slices achieve high performance, with a typical purity exceeding 95% and completeness above 90% for contained neutrino interactions [13].

3.1.2 Cluster Formation and 3D seeding

MINERvA planes are organized in three views (X, U, V), rotated by 60° with respect to one another (see Fig. 2.2.1). Within a time slice, spatially adjacent hits in a given view are grouped into *clusters*. Each cluster is characterized by:

- a centroid (s_{view}, z),
- a total visible energy $E_{\text{cl}} = \sum E_{\text{hit}}$,
- and a time t_{cl} (energy-weighted).

Pairs/triplets of 2D clusters that are geometrically and temporally consistent are combined to form *3D seeds*. Seeds provide starting parameters for track and shower pattern recognition.

3.1.3 Track Reconstruction

Charged particle trajectories are first identified separately in each of MINERvA's 2D views. A line-finding algorithm, based on the Hough transform [38], searches for sets of clusters that line up approximately straight within a view. The idea is that each possible straight line is represented by a point in a "parameter space," and clusters that fall along the same line cause the algorithm to accumulate

votes at that point. In this way, even with noise or missing hits, the straight-line paths of charged particles can be recognized.

Once candidate straight tracks are found in the X, U, and V views, they are combined to form 3D track candidates. These are then refined with a Kalman filter [35], which follows the particle plane by plane through the detector. At each step the filter keeps a compact description, called the *state vector*, containing the particle's position, direction, and momentum. The state vector is updated whenever new measurements are added, while also accounting for the physical effects that can change the trajectory, such as multiple Coulomb scattering (small random deflections from nuclei) and gradual energy loss.

The optimal track parameters are those that minimize the difference between the measured clusters and the predicted track positions, weighted by the expected measurement uncertainties.

Direction disambiguation. The track's forward direction is determined either by (i) matching a through-going muon track into the downstream MINOS Near Detector (Sec. 3.1.5), or (ii) identifying the Bragg peak in dE/dx (the rise in energy loss at the end of a stopping proton track). Correct direction assignment is essential for proton identification and for measuring the opening angle in two-proton events.

Track quality and "nodes". A *node* is a detector plane that contributes a cluster to a reconstructed track. A minimum number of nodes per track is required (analysis-dependent) to ensure robust momentum and dE/dx estimates. Additional constraints on the continuity of nodes (few or no large gaps) suppress false tracks from noise or accidental hit combinations.

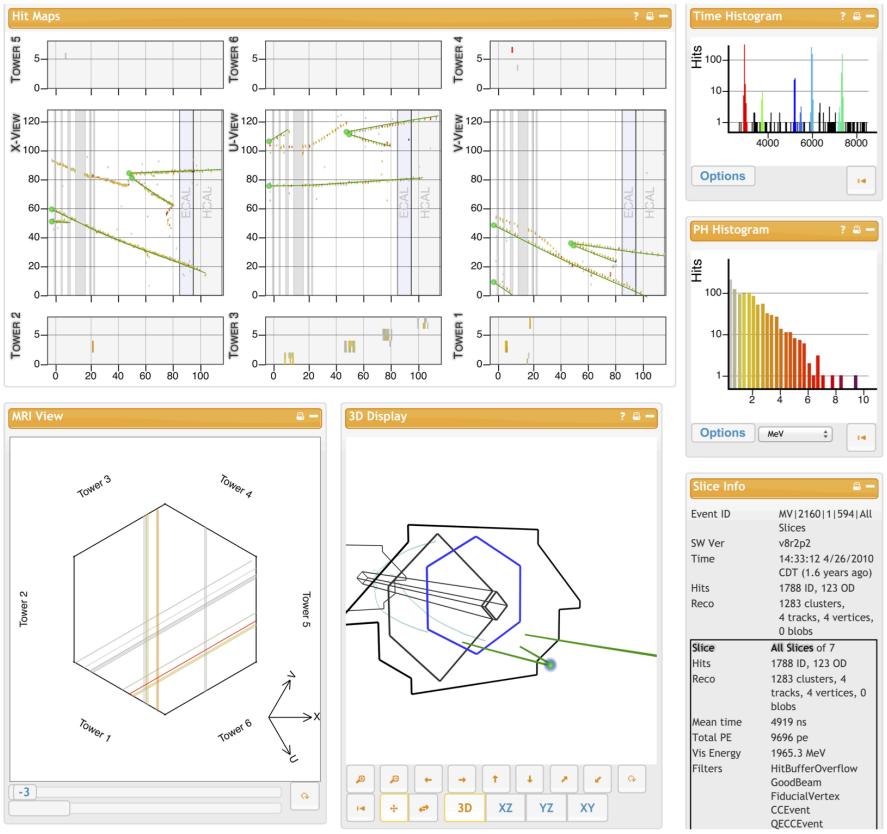

Figure 3.1: Illustration of view–space clustering and 3D track building with node assignments, adapted from[61]. This display corresponds to a *full NuMI spill* rather than a single interaction. The *top-right* panel highlights the time-slicing stage: multiple slices (distinct in-time clusters within the spill) are visible in this view, from which individual slices are then promoted to 3D event candidates for subsequent reconstruction.

3.1.4 Vertex Reconstruction

Reconstructed tracks within a time slice are extrapolated upstream to find a common point of closest approach. A robust, iterative vertex fit minimizes the sum of transverse distance significances:

$$\min_{\mathbf{r}_v} \sum_i \frac{d^2_{\perp,i}(\mathbf{r}_v)}{\sigma^2_{\perp,i}},$$

with outlier down-weighting to handle secondaries and spurious stubs. The vertex covariance is propagated from the track covariances, enabling vertex-based quality selections and fiducial volume enforcement.

3.1.5 Muon Reconstruction and MINOS Matching

Muon candidates are long, minimally ionizing tracks exiting downstream. For such tracks, a geometrical and timing match is attempted to a MINOS-ND track:

- *Spatial*: The extrapolated endpoint from MINERvA to the MINOS front face must fall within $\sim$20 cm of the matched MINOS track projection in the transverse plane; 3D angular consistency within $\sim 5^\circ$ is also required.
- *Timing*: The time difference $|t_{\text{MINOS}} - t_{\text{MINERvA}}|$ must be less than $\sim$20 ns, ensuring correct bunch identification and rejecting accidental coincidences.

A successful match provides charge sign and momentum via curvature in the MINOS magnetic field. For un-matched muons, alternative strategies are applied: fully contained muons use range in MINERvA, while exiting but un-matched muons rely on calorimetric energy estimation with multiple Coulomb scattering (MCS) constraints.

The overall track-to-track matching efficiency for muons exiting MINERvA into MINOS is approximately 98% for tracks above 1 GeV/c, with residual inefficiencies dominated by geometric acceptance and occasional detector dead channels [13].

3.1.6 Calorimetric Objects: EM and Hadronic Showers

Clusters not associated with tracks are grouped into topological showers using nearest-neighbor and directionality criteria. EM showers are identified by compact, rapidly growing longitudinal profiles

and view-coherent transverse spreads; hadronic showers are more diffuse. Calorimetric energies are reconstructed by applying view- and region-dependent sampling fractions:

$$E_{\mathrm{vis}} = \sum_{\mathrm{clusters}} E_{\mathrm{cl}}, \qquad E_{\mathrm{cal}} = C_{\mathrm{region}}\, E_{\mathrm{vis}},$$

with C_{region} derived from through-going muons, test-beam calibration, and simulation. For $\pi^0 \to \gamma\gamma$ candidates, two EM clusters with a common vertex are used to compute an invariant mass hypothesis. The calorimetric reconstruction, including determination of sampling fractions and validation with test-beam data, is described in detail in Refs. [13,24].

3.1.7 Hadron dE/dx and Proton Identification (PID)

For each track, the per-plane (or per-node) dE/dx is compared to expected Bethe–Bloch profiles for proton, pion, and muon hypotheses. We construct a log-likelihood ratio (LLR) using truncated-mean dE/dx to reduce Landau tails:

$$\mathrm{LLR}_{p/\pi} = \sum_{n \in \mathrm{nodes}} \ln \frac{P\Big((dE/dx)_n \mid p, \hat{\beta}\gamma_n\Big)}{P\Big((dE/dx)_n \mid \pi, \hat{\beta}\gamma_n\Big)}.$$

Tracks with $\mathrm{LLR}_{p/\pi}$ above an analysis-tuned threshold are identified as protons. A separate $\mathrm{LLR}_{p/\mu}$ can be used to suppress misidentification of minimum-ionizing tracks.

Figure 3.2 illustrates $\mathrm{LLR}_{p/\pi}$ distributions for leading (left) and subleading (right) protons. Higher scores correspond to tracks with energy-loss profiles consistent with protons, while lower scores correspond to pion-like hypotheses.

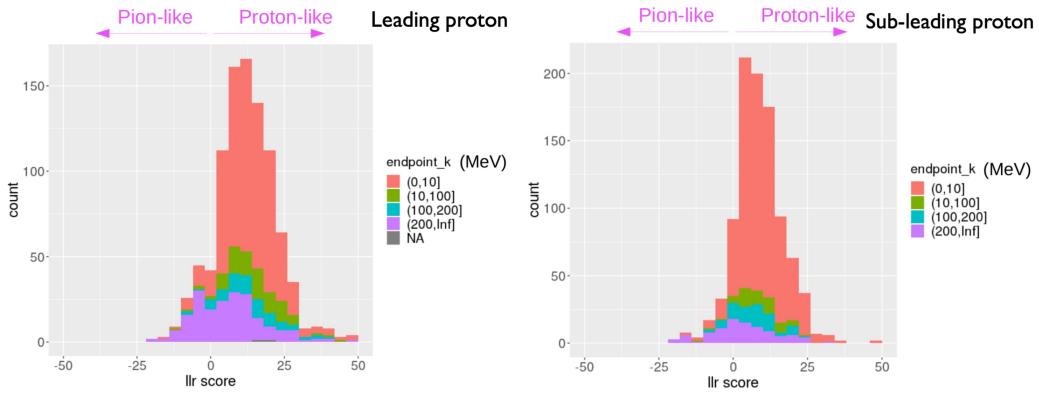

Figure 3.2: Example of $\mathrm{LLR}_{p/\pi}$ distributions for leading (left) and subleading (right) proton candidates. The distributions are separated into components by endpoint kinetic energy. Higher LLR values indicate proton-like behavior.

Additional PID variables and selection usage. The LLR method described above provides the most detailed dE/dx-based proton identification and is explicitly used in the `CCQENuLLR` cut to suppress pion contamination. Earlier cuts in the selection chain (`CCQENuSingleProton`, `CCQENuExtraProtons`, and `CCQENuExtraTracksProtons`) employ a simpler scalar PID variable known as the *proton score*, developed within the CCQENu framework. Both approaches rely on the same physical principle—comparison of measured energy loss to expectations for different particle hypotheses—but the LLR provides a higher-fidelity, spline-based likelihood comparison using per-node information.

Momentum by range and the ESC selection. Contained protons use range to estimate kinetic energy T_p via a range–energy map $R(T_p)$ obtained from simulation and test-beam tuning. To improve momentum resolution and suppress inelastic scatters, we apply *Elastically Scattering Contained* (ESC) criteria: the terminal segment must show a rising Bragg peak and no evidence for inelastic interactions (e.g., sudden kinks or anomalous energy deposition). ESC-selected protons have superior momentum-by-range performance; tuned ESC cuts used in this analysis are documented in Sec. 4.2.

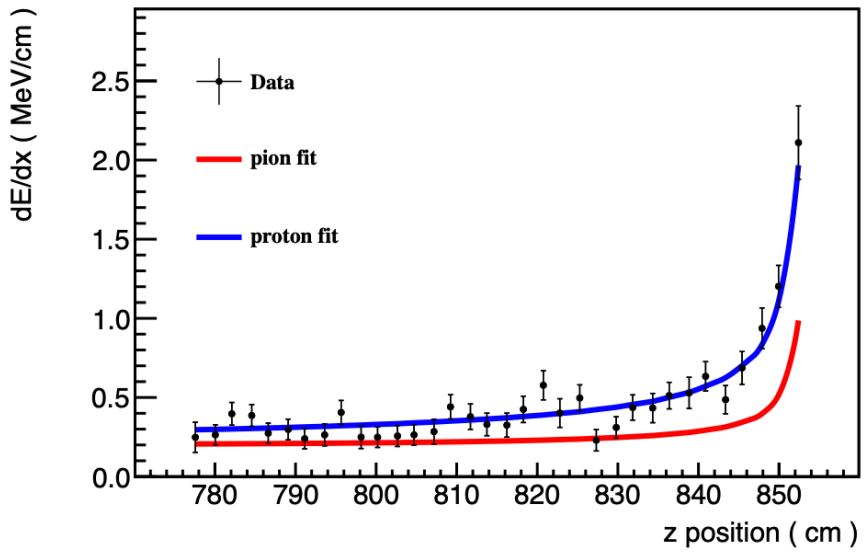

Figure 3.3: Typical dE/dx profile for a clearly identified proton candidate in the data (Fig. 44 in[13]).

3.1.8 Michel Electron Tagging and "Blob" Counting

Delayed electrons from $\pi^{\pm} \to \mu^{\pm} \to e^{\pm}$ decays (*Michel electrons*) are a powerful handle on pion contamination in CC 0π-like selections. We search for delayed clusters within a spatial cone around the primary vertex (or the downstream end of a short track) and in a delayed time window (e.g. $\mathcal{O}(\mu s)$ after the main event). A positive tag sets the *Michel cut* used to define sidebands and suppress pion-containing backgrounds.

We also count *blobs*: isolated, track-detached energy clusters near the vertex beyond what is expected from two protons and a muon. A high number of blobs often indicates additional hadronic activity (e.g. π production or FSI). The *Number of Blobs* cut and its sideband usage are described in Sec. 4.3.

3.1.9 Fiducial, Containment, and Geometry Effects

Fiducial volume. Throughout this work, the *fiducial volume* for reconstructed vertices is the MINERvA scintillator tracker, defined by $5980 < z < 8422$ mm along the beam axis and a regular hexagon of apothem 850 mm transversely. Vertices must lie inside this region; periods with known readout issues are removed by standard dead-time/data-quality flags. The same geometric boundaries are used to define the Monte Carlo truth region employed later for efficiencies and acceptances (see Chapter 4).

Containment and tracking considerations. Accurate momentum-by-range estimates for protons rely on tracks that range out within the tracker. In practice, containment and minimum hit/plane multiplicity are the dominant geometric factors controlling whether a reconstructed track achieves good resolution. The precise selection criteria and their efficiencies are presented in Secs. 4.1–4.2.

Angular acceptance features. Because the active planes are oriented in X, U, and V stereo views ($0°$, $\pm 60°$), the per-plane hit pattern depends on track polar angle. Tracks emitted roughly $70°$–$110°$ to the beam tend to leave fewer hits per plane and exhibit more frequent pattern ambiguities, which reduces reconstruction efficiency and resolution in that band. This geometric effect is accounted for in the analysis via phase-space limits and efficiency corrections (see Chapter 4).

3.1.10 Timing, Cosmic Rejection, and Dead Time

Tight intra-slice timing and topology vetoes reduce out-of-time backgrounds. Dedicated cosmic tags (external muon counters when available, plus topology/timing templates) suppress cosmics during the spill. A *dead-time cut* removes periods of abnormal readout or known DAQ inefficiency, as tracked by standard run quality flags.

3.1.11 Reconstruction Systematics and Validation

Reconstruction contributes a set of analysis-level systematics:

- **Energy scale and response:** Uncertainties in the PE $\rightarrow$ MeV calibration, time dependence, and non-linearity propagate to hadronic and proton energies.
- **Tracking/vertexing:** Alignment, hit efficiency, cluster merging/splitting, and MCS modeling impact angular variables and vertex position.
- **PID and model dependence:** The dE/dx PDFs used in the LLR depend on material and step size; truncation choices introduce small biases. ESC criteria trade efficiency for purity and induce kinematic-dependent acceptance effects.
- **Containment/acceptance:** Geometric edge effects and the θ-dependent hit density affect node counts and pattern recognition performance.

We validate reconstruction with control samples: through-going muons for energy scale and alignment; stopping muons and protons for range–energy checks; photon conversions and EM showers for EM scale; and sidebands (Michel, blob) for background topology modeling. The simulation chain (Sec. 3.2) mirrors the full reconstruction to enable response-matrix construction and data–MC closure tests used later in unfolding.

The definitions above connect directly to the analysis selections used later:

- *MINOS-matched events* (Sec. 3.1.5),
- *Reconstructed proton multiplicity* ≥ 2 with *node* and *ESC* quality cuts (Sec. 3.1.7),
- *Proton PID cuts* using $\mathrm{LLR}_{p/\pi}$ (Sec. 3.1.7),
- *Michel cut* and *Number of Blobs cut* (Sec. 3.1.8),

- *Signal cut* (truth-level definition) applied in MC only, used for efficiency and migration matrices (defined later),
- *Dead time cut* (Sec. 3.1.10),
- *Helicity cut* selecting the correct beam polarity spill,
- *LLR score and track–vertex distance cuts* (Sec. 3.1.7, 3.1.4).

These pieces together deliver the two-proton, no-pion signal topology with high purity and stable kinematic reconstruction, forming the basis for background tuning, unfolding, and cross-section extraction in subsequent chapters.

3.2 Detector Simulation

A faithful detector simulation is essential for interpreting MINERvA measurements, deriving detector efficiencies and acceptances, and propagating systematic uncertainties. The MINERvA simulation chain integrates (i) a detailed geometry and materials model of the detector, (ii) particle transport and interactions in matter using GEANT4 [12,16], (iii) an optical photon and readout digitization model tuned to data, and (iv) time-dependent overlays and calibrations to reproduce the detector's evolving conditions during data taking. The simulation is validated with in situ control samples and with dedicated test-beam measurements, and the full chain is documented in the MINERvA NIM paper [13].

3.2.1 Overview of the Simulation Chain

The end-to-end workflow proceeds as follows:

1. **Neutrino flux** & **interaction generation:** The on-axis NuMI flux is modeled using the beamline simulation (G4NUMI) constrained by hadron production data [10,15]. Neutrino inter-

actions with detector materials are generated with a neutrino event generator (e.g., GENIE), producing a list of final-state particles entering the detector volume.

2. **Geant4 transport:** Final-state particles and all secondaries are tracked through a detailed Geant4 model of MINERvA [12,16,13], including electromagnetic and hadronic processes, multiple scattering, energy loss, and hadronic cascades in passive and active media.

3. **Optical response and digitization:** Energy deposits in scintillator are converted to scintillation light with quenching (dL/dx vs. dE/dx), transported via wavelength-shifting (WLS) fibers with realistic attenuation and reflections, converted to photoelectrons at the multi-anode PMTs, and then processed through a model of the front-end electronics (gain, shaping, thresholds, cross talk, and channel-to-channel variations).

4. **Time-dependent overlays:** Random-trigger data (out-of-time activity and on-spill backgrounds) are overlaid to emulate pile-up, dark noise, and accidental activity, reproducing data-taking conditions run-by-run.

5. **Reconstruction and analysis:** The simulated hits undergo the *same* reconstruction chain as data (see 4) to enable direct, like-for-like comparisons and to derive migration matrices, efficiencies, and detector systematics.

3.2.2 Geometry and Materials Model

The Geant4 geometry follows the as-built survey of the detector [13], including:

- **Active planes:** Triangular polystyrene scintillator strips with co-extruded TiO_2 reflective coating, arranged in X, U, V stereo planes (60° rotations).

- **Passive media:** Precise maps of nuclear targets (C, Fe, Pb, water, He), lead (ECAL), steel (HCAL), structural supports, readout frames, and upstream/downstream shielding.

- **Services and dead material:** PMT boxes, light guides, optical connectors, and electronics, all modeled at the level needed to reproduce shower containment and energy losses.

Material densities and thicknesses are varied within survey uncertainties to define geometry systematics (Sec. 3.2.6).

3.2.3 Optical Photon and Digitization Model

Energy deposits in scintillator are converted to visible light with a non-linear response at high specific ionization. The simulation implements:

1. **Scintillation yield and quenching:** Light yield is modeled as a function of dE/dx (Birks-like quenching), with parameters tuned to through-going muons and proton stopping power. A generic form is

$$\frac{dL}{dx} = S \frac{dE/dx}{1 + k_B \, dE/dx},$$

   where S is the intrinsic scintillation yield and k_B is the Birks parameter (both tuned within the ranges reported in [13]).

2. **WLS transport and attenuation:** Scintillation photons are captured by the WLS fiber embedded in each strip and transported to the optical connector. Attenuation is modeled with a double-exponential profile (short/long components) with reflectivity at the mirrored far end; parameters are constrained by bench measurements and in situ muon scans [13].

3. **Photo-statistics and MAPMT response:** The mean number of photoelectrons (PE) at the photocathode is converted to a charge signal with Poisson statistics, channel-dependent gain, and cross talk. Non-linearity and saturation effects are included where relevant. Channel equalization and absolute PE scale are anchored to muon MIP peaks in data [13].

4. **Electronics shaping and thresholds:** Pulse shaping, digitization, zero suppression, and time-stamping are simulated to reproduce time and charge spectra, including per-channel thresholds and noise.

3.2.4 Time Dependence, Pile-Up, and Conditions

Detector conditions (gain, light yield, channel health) evolve over long data-taking periods. The simulation incorporates:

- **Run-dependent calibrations:** Time-binned gain and channel-status maps from data quality monitoring are applied to MC, reproducing the slow drifts and discrete interventions documented in [13].
- **Random-trigger overlays:** To emulate out-of-time activity, accidental hits, and on-spill pile-up, zero-bias data are overlaid onto MC hits with the same spill structure as data, matching the occupancy and noise spectra [13].

3.2.5 Validation and Tuning

The detector simulation is validated using a hierarchy of benchmarks:

1. **Minimum-ionizing muons:** Data/MC agreement of MIP peak position and width across planes and angles is used to validate absolute light yield and strip-by-strip equalization [13].
2. **Michel electrons:** The Michel electron energy spectrum and spatial distributions validate the low-energy EM response and timing.
3. **Stopping protons:** Range–energy and dE/dx profiles for stopping protons validate quenching and hadronic ionization modeling.

4. **Electromagnetic & hadronic showers:** The response and resolution to electrons/pions are cross-checked against the MINERvA test-beam program and in situ samples; calorimetric constants and sampling fractions are tuned within uncertainties [13].

3.2.6 Detector Systematic Variations

To propagate detector modeling uncertainties into unfolded cross sections, we evaluate a set of alternative simulations ("universes") varying:

- **Optical model:** global light yield, Birks constant k_B, WLS attenuation lengths and mirror reflectivity, and MAPMT gains and cross talk.
- **Geometry/materials:** strip dimensions, passive material densities, target thicknesses, and small plane-to-plane alignment shifts within survey bounds.
- **Electronics:** thresholds, noise spectra, and zero-suppression parameters.
- **Time dependence:** alternative time-binning and drifts in gain/light yield.

Each universe is reconstructed identically to nominal MC and data, and its effect is carried through background constraints, unfolding, and efficiency/acceptance corrections (cf. Ch. 4). The covariance from these variations is combined with flux and interaction-model systematics to form the total uncertainty budget.

In summary, the MINERvA detector simulation combines a detailed geometry and materials description with a tuned optical/digitization model and time-dependent overlays. Validation against control samples and test-beam benchmarks [13] underpins the reliability of detector corrections used throughout this analysis.

The secret of success in research is constancy to purpose.

Peter Kropotkin

4

Analysis

The aim of the MINERvA experiment is to produce measurements that advance our understanding of interactions between neutrinos and nuclei. Much of this understanding comes from comparisons with results of other experiments and/or predictions of available theoretical models. Thus, it is vital to ensure that measurements are as free from detector or simulation artifacts as possible to facilitate these comparisons while preserving valuable information about the studied phenom-

ena.

It is standard practice to report measurement results in the form of a differential cross-section as a function of an observable kinematic variable:

$$\frac{d\sigma}{dX_i} = \frac{\sum_j U_{ij}(N_j^{\text{measured}} - N_j^{\text{background}})}{\varepsilon_i(T\Phi_i)\Delta X_i} \tag{4.1}$$

where $N_j^{\text{measured}} - N_j^{\text{background}}$ represents the number of signal events in detector bin j, after subtracting the estimated background contribution. The unfolding matrix U_{ij} corrects for detector smearing effects and maps the reconstructed distribution into the "true" distribution. The efficiency factor ε_i accounts for detection efficiency and acceptance corrections, while T represents the number of target nucleons in the fiducial volume of the detector. The flux Φ_i corresponds to the incident neutrino flux, and ΔX_i is the bin width of the chosen observable variable.

Cross-section measurements in neutrino experiments generally proceed through a sequence of steps designed to extract the true underlying interaction rates while accounting for detector effects and systematic uncertainties. This analysis follows a well-established methodology consisting of the following key stages:

1. **Event Selection**: The dataset is subjected to a set of selection criteria to isolate neutrino interactions of interest while minimizing contamination from background processes. These selection cuts are optimized to balance signal efficiency and purity, reduce systematic uncertainties, and improve kinematic reconstruction accuracy. The selected events are then organized into kinematic bins, forming the basis for further analysis.

2. **Background Subtraction**: After applying selection cuts, background events—interactions that pass the selection criteria but are not true signal events—must be removed. This is accomplished using Monte Carlo (MC) simulations, which provide an estimate of the ex-

pected background contribution. Since the accuracy of the MC-based background estimation is limited by model uncertainties, additional constraints are applied using sideband samples. These sidebands are selected to be kinematically close to the signal region but enriched in specific background processes, allowing us to derive data-driven corrections to the background prediction. In particular, sidebands are used to tune the normalization of different background components before subtraction, reducing systematic biases and improving the reliability of the extracted signal.

3. **Unfolding**: Due to limitations in detector resolution and event reconstruction, measured kinematic variables may differ from their true values. This smearing effect is corrected using an unfolding procedure, which applies an unfolding matrix derived from simulation to transform the reconstructed distribution into the true interaction distribution.

4. **Efficiency and Acceptance Corrections**: Not all neutrino interactions in the fiducial volume are detected due to geometric constraints and detector inefficiencies. The efficiency-corrected cross-section is obtained by applying a correction factor, computed as the ratio of selected signal events to the total simulated signal events, ensuring that the measurement accurately represents the full set of interactions.

5. **Normalization**: The final step involves normalizing the cross-section by the total neutrino flux and the number of target nucleons within the fiducial volume. Additionally, bin widths are accounted for to produce a properly scaled differential cross-section measurement with units of $[cm^2/\text{target nucleon}]/[\text{variable unit}]$.

A dedicated software framework[48] was developed by MINERvA collaboration to process the data through each stage of this analysis. Its final output is *a set of three single-differential cross-section distributions* as functions of key kinematic observables (listed in 4.1).

Parallel to the data cross-section extraction, a Monte Carlo (MC) simulation is processed through the same analysis pipeline. The MC simulation plays a dual role: first, it provides the necessary corrections for background estimation, unfolding, efficiency, and acceptance adjustments; second, it serves as a benchmark for data-Monte Carlo comparisons at each stage of the analysis.

The MC-generated distributions undergo the same selection cuts, binning, and cross-section extraction as the experimental data, ensuring consistency in event processing. By applying identical analysis procedures to both data and MC, we validate the impact of detector effects and modeling assumptions. This approach ensures that the final extracted differential cross sections are directly comparable to theoretical predictions and results from other experiments, providing a meaningful context for interpretation.

4.1 Signal definition

The signal definition serves two purposes: it specifies the underlying physics final state we intend to measure (at truth level), and it limits the measurement to a region of phase space where the detector and reconstruction perform reliably. The latter balances statistical reach against systematic uncertainties from acceptance and reconstruction.

Truth-level signal (physics definition)

An event is part of the signal if, at generator truth level, it satisfies:

- charged-current muon-neutrino interaction: $\nu_\mu + A \to \mu^- + X$ (CC),
- exactly two final-state protons exiting the nucleus: $n_p = 2$,
- no final-state pions exiting the nucleus: $n_\pi = 0$.

This definition is independent of detector response and reconstruction and is meant to be comparable across experiments and generators.

Phase-space (analysis) constraints

To ensure robust reconstruction and well-controlled systematics, we further restrict the signal to the following truth-level kinematic region:

- muon polar angle with respect to the beam: $\theta_\mu < 20°$,
- for each proton counted in the measurement: $\theta_p < 70°$ or $\theta_p > 110°$,
- proton energy threshold: $E_p > 1063.27$ MeV, corresponding to a kinetic energy $T_p > 125$ MeV or momentum $p_p > 0.48$ GeV/c.

These are the same phase-space limits used to define the fiducial "visible" region for the unfolding and efficiency corrections. They ensure that the muon can be MINOS-matched and that selected protons have sufficient range and light yield to be reconstructed with good efficiency.

Implementation note (selection vs. definition)

The truth-level items above define the *signal*. Practical event selection also applies detector/reconstruction requirements (e.g., a negative, through-going muon and successful MINOS matching). These are not part of the signal definition, but rather of the *event selection* used to isolate the signal sample and to compute efficiencies. The analysis is performed on three-track events ($\mu^- + 2p$ candidates) passing the selection, and then corrected to the truth-level definition via background subtraction, unfolding, and efficiency/acceptance corrections.

When more than two protons are reconstructed, the two most energetic ones are selected for analysis. The more energetic of the two is designated as the *leading proton*, and the less energetic as

the *subleading proton*.

Measured observables

We report single-differential cross sections for:

1. $\cos(\theta_{pp})$ — the lab-frame measured opening angle between the two protons,
2. p_{leading} — the momentum of the higher-momentum (leading) proton,
3. $p_{\text{subleading}}$ — the momentum of the lower-momentum (subleading) proton.

The "leading" and "subleading" labels are assigned using reconstructed proton momenta, with migrations corrected by the unfolding procedure (see 4.4).

4.2 Event Selection

At this stage of the analysis, a series of reconstructed-level cuts are applied to select events consistent with the truth-level signal definition (Sec. 4.1). The selection procedure follows the structure of the CCQENu analysis package, later integrated into the MINERvA Analysis Toolkit (MAT), which provides a validated framework for event filtering and quality control. Most of the algorithms were originally developed by the MINERvA collaboration, while the elastically scattering contained (ESC) proton selection was tuned specifically for this analysis.

Two optimized selections were implemented: one used for the measurement of the proton–proton opening angle $\cos(\theta_{pp})$, and another for the proton momentum spectra. The latter applies additional cuts to ensure the accurate reconstruction of proton momenta.

Summary of cuts

The following list describes each selection requirement in the order it is applied:

- **AnaTool (preselection).** A general event-quality requirement ensuring that each event is successfully reconstructed within the standard analysis framework and passes all basic detector integrity and timing checks.

- **Muon angular cut.** Require the reconstructed muon polar angle relative to the beam to satisfy $\theta_\mu < 20°$. This ensures that the muon exits toward the downstream MINOS Near Detector, enabling reliable charge-sign and momentum reconstruction.

- **MINOS match.** The reconstructed MINERvA muon candidate must be geometrically and temporally matched to a corresponding track in MINOS, providing an independent measurement of the muon's momentum and charge. This suppresses misreconstructed or misidentified muons.

- **Deadtime removal.** Events recorded during brief periods when the detector was not fully responsive (e.g., during electronics readout or synchronization gaps in the data acquisition system) are removed. This ensures consistent detector performance over the entire dataset.

- **Muon charge sign.** Only events with a reconstructed negatively charged muon (μ^-) are retained, isolating ν_μ charged-current interactions and removing the small antineutrino component.

- **Two reconstructed proton candidates.** Events must contain at least two reconstructed proton tracks emerging from the interaction vertex, each with valid fits and particle-identification (PID) information. When more than two proton-like tracks are reconstructed, the two with the highest reconstructed kinetic energies are selected for analysis and referred to as the *leading* and *subleading* protons. This convention, following earlier MINERvA CCQE-like analyses [54], preserves efficiency against reconstruction-induced extra tracks while maintaining consistency with the truth-level definition of the exclusive $\mu^- + 2p$ topology.

- **Single-proton PID threshold (CCQENuSingleProton).** The leading proton candidate must have a PID (*proton score*, defined in Sec. 3.1.7 and originally introduced in [13]) above a Q^2-dependent threshold, typically between 0.1 and 0.2 in the medium-energy configuration. This ensures that the leading proton is well identified and reduces pion contamination.

- **Extra-proton veto (CCQENuExtraProtons).** Any additional reconstructed proton-like tracks must have sufficiently high proton scores. Tracks failing these criteria are treated as mesonic or spurious and cause the event to be rejected, removing inelastic events with extra nucleons or pions.

- **Extra-track veto (CCQENuExtraTracksProtons).** Events containing extra nonproton tracks (PID score < 0.25) are removed, further isolating the exclusive $\mu^- + 2p$ final state.

- **Recoil-energy cut (SignalF).** The total visible energy outside reconstructed tracks and the vertex region,

$$E_{\text{recoil}} = E_{\text{nonvtx\_iso\_blobs}} + E_{\text{dis\_id}},$$

  must satisfy $E_{\text{recoil}} < 500$ MeV for single-track and < 550 MeV for multitrack events. This suppresses events with excess neutral energy from photons, neutrons, or pion decays.

- **Track–vertex distance cut.** The reconstructed starting point of the proton track must lie within 150 mm of the reconstructed interaction vertex:

$$\Delta r_{\text{vtx}} < 150 \text{ mm}.$$

  This ensures a consistent vertex topology and rejects tracks produced by secondary interactions.

- **Log-likelihood PID (LLR) cut.** Both reconstructed protons must have positive log-likelihood

ratios, $\mathrm{LLR}_{p/\pi} > 0$, as computed using the spline-based likelihood PID tool. This strongly reduces pion contamination and ensures both tracks are proton-like.

- **Elastically Scattering Contained (ESC) selection.** Proton tracks are required to exhibit an energy-deposition pattern consistent with purely elastic scattering—characterized by a smooth rise in dE/dx toward a Bragg peak at the stopping point and the absence of secondary interactions along the track. Node-normalized energy variables were examined sequentially, beginning with $(E_0 + E_1)$, which is sensitive to proper reconstruction of the track start. Subsequent thresholds were tested on later nodes (E_2, E_3, E_4, E_5) to identify well-contained, smoothly stopping protons. At each step, the cuts were tuned to balance sample purity and statistical retention, ensuring that the selected events exhibit both consistent energy deposition and reliable momentum reconstruction. The resulting composite ESC criteria are:

$$(E0 + E1)_{leading} > 12, \quad E2_{leading} > 6, \quad (E0 + E1)_{subleading} > 6,$$

for the leading and subleading protons, respectively. These selections preferentially retain contained, elastically scattered protons and significantly improve the momentum-by-range resolution.

Figure 4.1 shows the dependence of fractional momentum bias on node energy for both leading and subleading protons, illustrating used distributions and results of the ESC tuning.

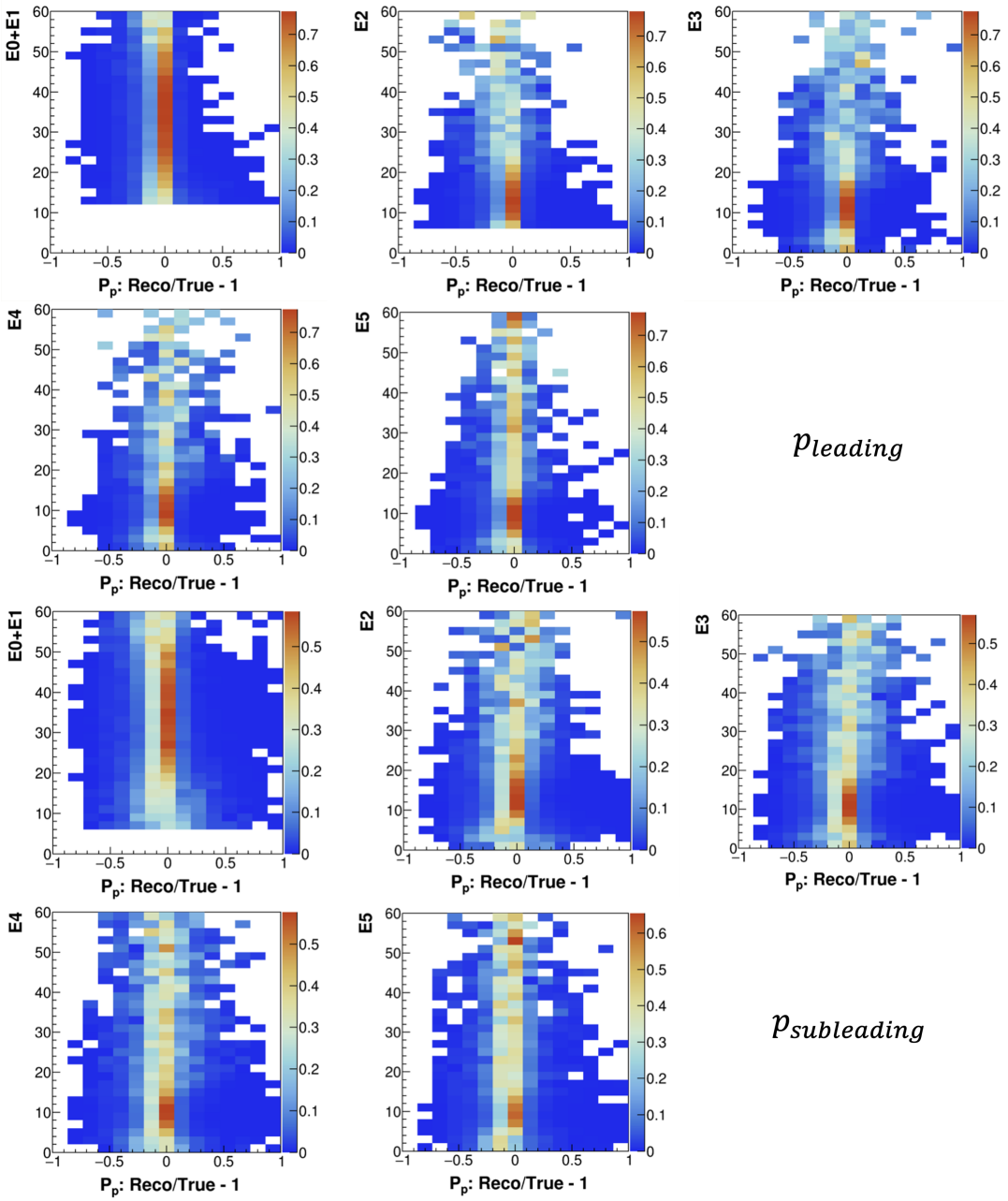

Figure 4.1: Effect of the ESC selection on proton momentum reconstruction, shown for the full exposure (Full POT). Each 2D histogram displays the distribution of $(p_{\text{reco}}/p_{\text{true}} - 1)$ versus node energy deposition ($E_0 + E_1, E_2, E_3$, E_4, E_5). The top row corresponds to leading protons and the bottom row to subleading protons. The ESC thresholds $((E0 + E1)_{leading} > 12, \quad E2_{leading} > 6, \quad (E0 + E1)_{subleading} > 6)$ were chosen to maximize momentum accuracy while maintaining acceptable signal efficiency.

- **Michel electron veto.** Events containing delayed clusters consistent with Michel electrons (from $\pi^{\pm} \to \mu^{\pm} \to e^{\pm}$ decays) are rejected.

- **Isolated-blob veto (NBlobs).** The number of nonvertex isolated clusters downstream of the vertex must be ≤ 1. Events with two or more such clusters are removed, as these typically indicate neutral-particle activity inconsistent with the no-pion signal definition.

4.2.1 Results of Event Selection

Table 4.1 summarizes the number of data and Monte Carlo events passing each cut at the full exposure of all playlists combined ("Full POT"), along with a detailed breakdown of efficiencies and purities for one representative playlist (minerva1M), which accounts for approximately 17% of the total simulated exposure.

Table 4.1: Event yields at each selection stage for the full dataset (Full POT) and for the representative `minerva1M` playlist (about 17% of total MC).

DataPOT: `1.0613617e+21` *MCPOT:* `4.9873209e+21`

Cut name	Full POT		1M playlist (MC)			
	Data events	MC events	MC events	%Eff	Rel.%Eff	Rel.%All
AnaTool (preselection)	4.671e6	1.844e7	3.310e6	97.89	97.89	97.67
Muon $\theta < 20°$	4.575e6	1.805e7	3.241e6	97.81	99.92	97.92
Has MINOS match	4.511 e6	1.767e7	3.155 e6	95.91	98.06	97.34
Deadtime	4.398e6	1.733e7	3.082e6	93.72	97.71	97.69
Muon charge sign	4.135 e6	1.625e7	2.891e6	91.24	97.36	93.81
Two reco protons	5.078e5	2.057e6	3.622e5	13.87	15.20	12.53
Single-proton PID	3.787e5	1.526e6	2.691e5	12.35	89.06	74.30
Extra-proton veto	3.146e5	1.271e6	2.243e5	11.28	91.32	83.36
Extra-track veto	2.739e5	1.092e6	1.925e5	11.20	99.25	85.84
Recoil-energy (SignalF)	1.175 e5	4.732e5	8.247e4	10.51	93.86	42.82
Vertex distance	1.031e5	4.124e5	7.173 e4	10.01	95.22	86.98
LLR PID	2.534e4	1.157 e5	1.989e4	7.69	76.82	27.73
ESC selection	1.848e4	8.811 e4	1.509e4	6.92	90.05	75.86
Michel veto	1.345e4	6.845e4	1.164e4	6.40	92.45	77.15
Isolated-blob veto	9.063e3	4.982e4	8.488e3	6.09	95.11	72.91

The combined selection across all playlists yields approximately 4.7 million data events and 18.4 million simulated events after the initial preselection. Following all selection requirements, the final $\mu^- + 2p$ no-pion sample with ESC cuts consists of 9063 data events and about 49820 Monte Carlo events with purity of about 50% and an overall efficiency of roughly 6-7%.

Figures 4.2 and 4.3 show data–MC comparisons for $\cos(\theta_{pp})$ and p_{leading}, respectively, after applying their respective event selections.

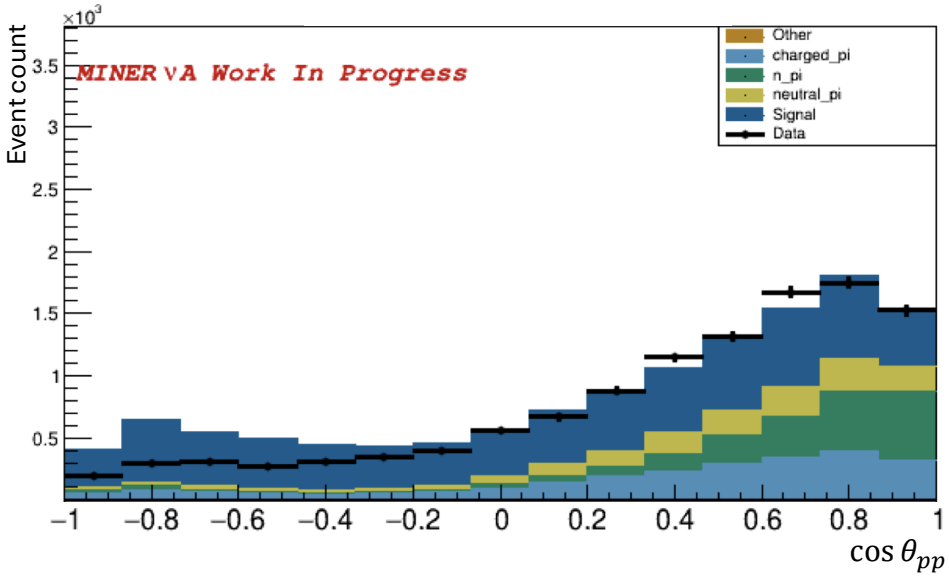

Figure 4.2: Distribution of $\cos(\theta_{pp})$, separated into true signal and three background categories based on GENIE final-state data. Note that an additional "Other" component initially appeared in the simulation but was found to be numerically small. Upon inspection of the associated events, all were reclassified into one of the existing categories listed above. Consequently, the "Other" component was eliminated from the final analysis without loss of completeness.

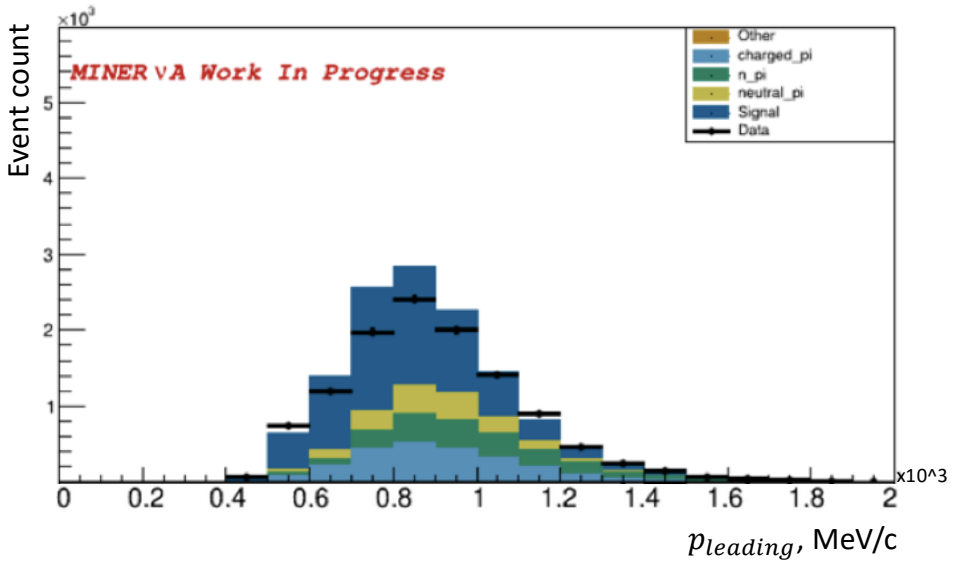

Figure 4.3: Distribution of p_{leading}, separated into true signal and three background categories based on GENIE final-state data. Note that an additional "Other" component initially appeared in the simulation but was found to be numerically small. Upon inspection of the associated events, all were reclassified into one of the existing categories listed above. Consequently, the "Other" component was eliminated from the final analysis without loss of completeness.

4.3 Background Subtraction

Even after applying the series of cuts described in previous sections, Monte Carlo (MC) simulations predict that a significant number of background events remain in the selected signal sample. The overall sample purity after the final selection is around 34% for ESC (4.1), and even less for event selection with no ESC cuts, indicating that background subtraction is an essential step of the analysis.

Figure 4.2 illustrates the predicted distribution of $\cos(\theta_{pp})$, separated into true signal and three background categories based on GENIE final-state data.

Before introducing the tuning procedure, it is important to discuss how background events can pass the selection and appear signal-like at the reconstructed level. In particular:

- Charged-pion events may pass if the pion is absorbed in the detector material, misidentified

as a proton, or if its decay electron (Michel) is not reconstructed.

- Events with neutral pions may pass if the photons convert early and the resulting electromagnetic showers are misidentified as blobs associated with protons.
- Multi-pion events can leak into the sample through combinations of pion absorption, misidentification, and incomplete reconstruction.

4.3.1 Background Classification and Tuning Strategy

The MC sample is categorized into four distinct truth-level components based on GENIE final-state interactions (FSI):

- **Signal:** true final state containing 2 protons and 0 pions.
- **Charged–pion background:** true final state containing exactly 1 $\pi^{\pm}$.
- **Neutral–pion background:** true final state containing exactly 1 π^{0}.
- **Multi–pion background:** true final state containing more than 1 π-meson of any charge.

An additional "Other" component initially appeared in the simulation but was found to be numerically small. Upon inspection of the associated events, all were reclassified into one of the existing categories listed above. Consequently, the "Other" component was eliminated from the final analysis without loss of completeness.

Each background component can contribute differently depending on the presence of Michel electrons or reconstructed blobs, which in turn reflect different underlying pion topologies. Accordingly, we introduced three sideband samples, each designed to constrain specific background types:

1. **Michel Sideband:** Events that pass all selection criteria except for the Michel electron veto. This sideband is enriched in events containing charged pions that decay to Michel electrons.

2. **Blob Sideband:** Events that fail the requirement on the number of reconstructed blobs, enhancing neutral-pion contamination.

3. **Michel-Blob Sideband:** Events that fail both the Michel and blob requirements, thus sampling a mix of charged- and neutral-pion backgrounds.

These sidebands, each dominated by different background compositions, provide complementary constraints for the tuning procedure (Figure 4.4).

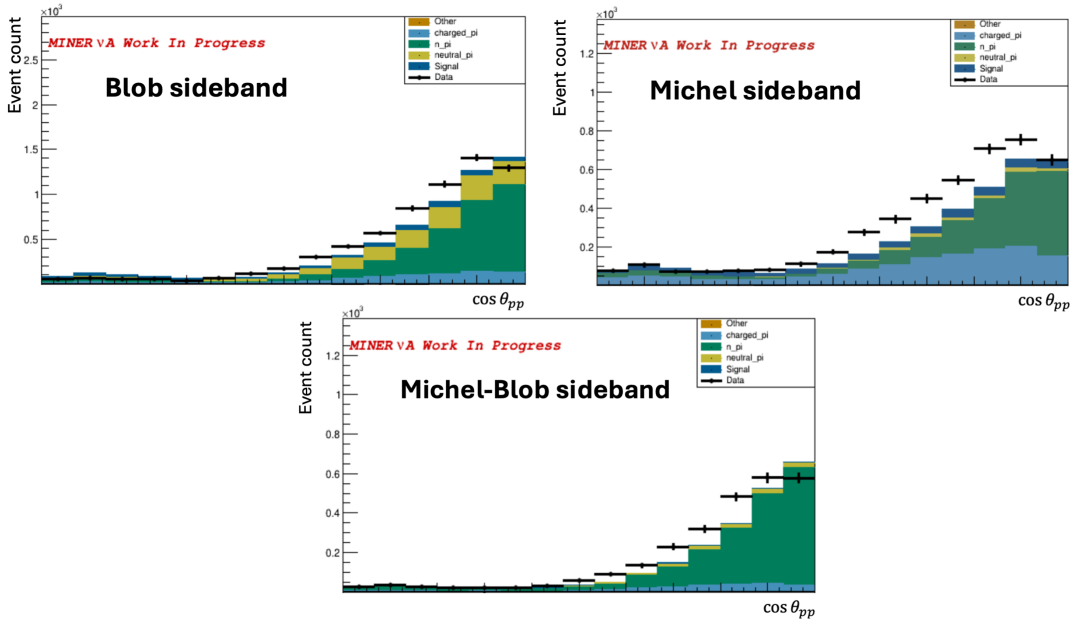

Figure 4.4: Distributions of $\cos(\theta_{pp})$ in three chosen sidebands, illustrating that they are background-dominated with minimal true signal contamination.

4.3.2 Iterative Fit Procedure

To determine optimal scale factors, we employ an iterative fit inspired by Singular Value Decomposition (SVD) unfolding. The fit simultaneously adjusts normalization factors for all four truth-level components—signal and three background types—across the signal region and the three sidebands by minimizing a combined χ^2 function:

$$\chi^2 = \sum_{i}^{N_{\text{bins}}} \frac{(N_{\text{MC},i} - N_{\text{data},i})^2}{\sigma^2_{\text{MC},i} + \sigma^2_{\text{data},i}}, \tag{4.2}$$

where $N_{\text{MC},i}$ and $N_{\text{data},i}$ represent the Monte Carlo and data counts in bin i, respectively, and σ denotes the corresponding statistical uncertainties.

Unlike a simple three-component background fit, we include an additional scale factor for the signal normalization. This accounts for small mismatches in the overall normalization between data and simulation due to beam flux and efficiency uncertainties. The four scale parameters (signal, $\pi^{\pm}$, π^0, and multi-pion) are updated iteratively until the global χ^2 reaches a stable minimum. Negative scaling factors are truncated to avoid unphysical solutions.

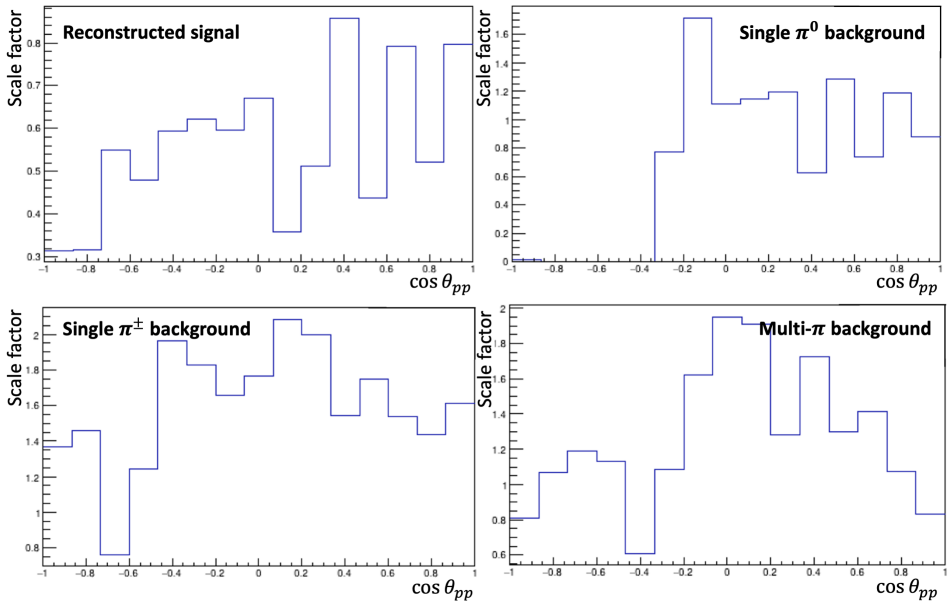

Figure 4.5: Scaling parameters (CV) for the four truth-level components across $\cos(\theta_{pp})$ bins.

4.3.3 Application of Background Scaling Factors

Once determined, the fitted scale factors are applied to the corresponding MC components. The tuned background prediction is then subtracted from the measured data in each bin, producing a background-subtracted signal distribution.

The post-fit agreement in $\cos(\theta_{pp})$ is shown in Figure 4.6. Agreement is nearly perfect in well-populated bins, with residual differences limited to the negative $\cos(\theta_{pp})$ region, where statistics are low.

4.3.4 Extension to Proton Momentum Variables

Given the robustness of the tuning in $\cos(\theta_{pp})$, the same scale factors were initially applied to the proton momentum distributions (p_{leading} and $p_{\text{subleading}}$). While this yielded reasonable agreement,

small systematic trends remained—most notably a linear discrepancy in the leading-proton momentum. This feature is evident in Figure 4.7 (see central region between [placeholder: 0.6–0.9 GeV/c]).

To mitigate this effect, we introduced a small linear correction to the most populated bins of the leading-proton distribution, re-ran the fit, and propagated the updated scale factors to the subleading-proton sample (Figure 4.8). The results demonstrate improved data/MC consistency across both variables.

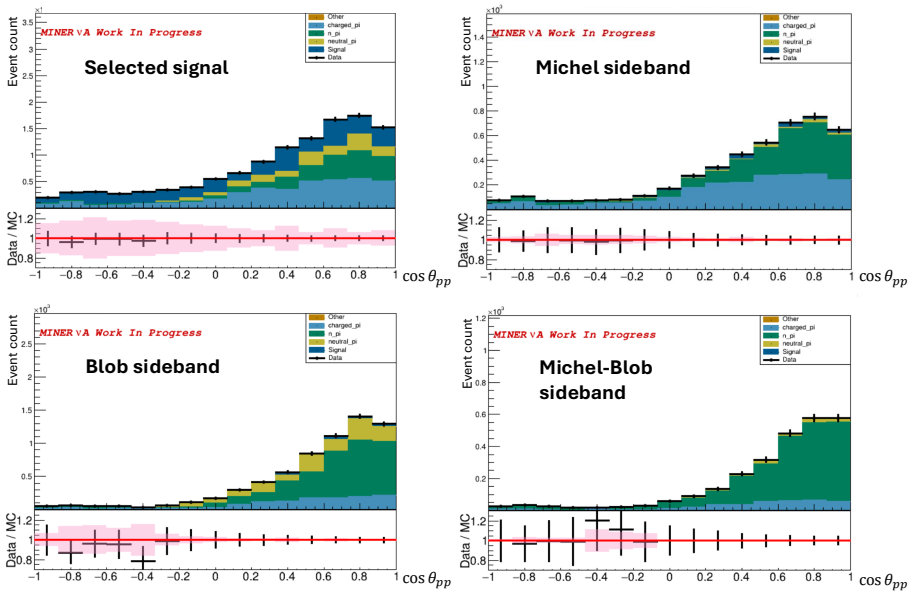

Figure 4.6: Distribution of $\cos(\theta_{pp})$ after background fit, separated into true signal and three background categories.

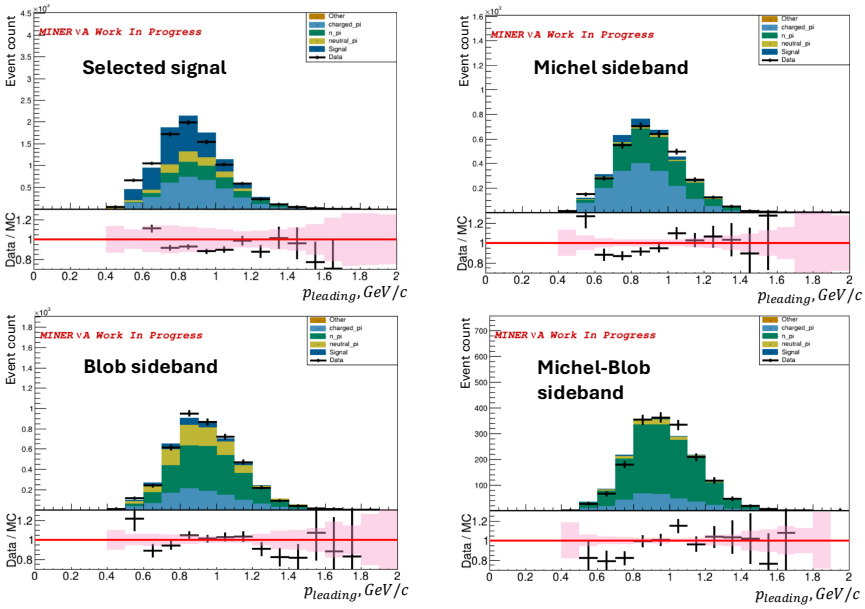

Figure 4.7: Distribution of p_{leading} after background fit, showing improved agreement in the 0.6–0.9 GeV/c region following the linear correction.

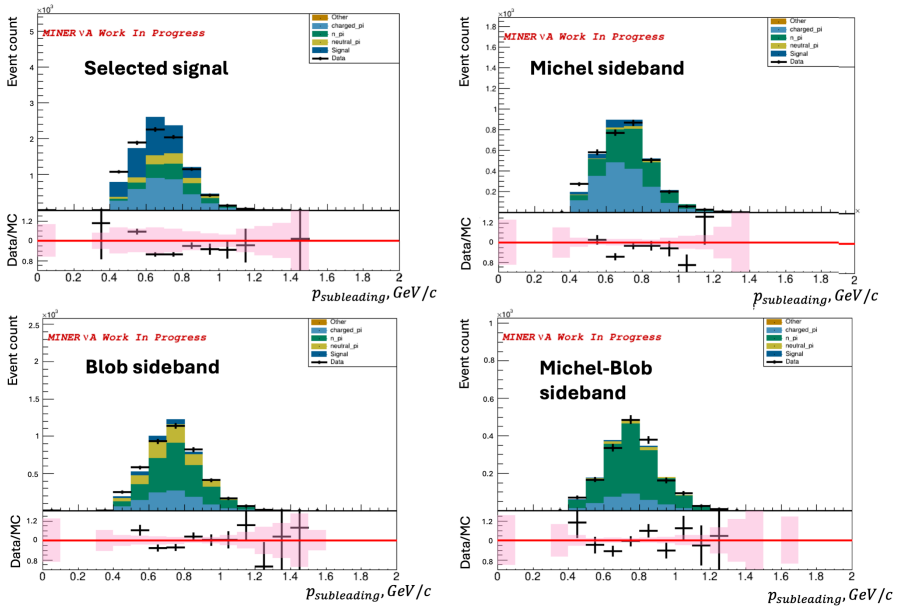

Figure 4.8: Distribution of $p_{\text{subleading}}$ after background fit, showing consistent tuning across both proton momentum observables.

4.3.5 Results of Background Subtraction

The primary goal of the sideband fit is to ensure an accurate description of the background model rather than to improve data–MC agreement in the signal region itself. Improved agreement across the tuned variables is, however, a natural byproduct of a more reliable background constraint.

Figures 4.6–4.8 show the tuned results for angular and momentum variables. After applying the final scale factors, the scaled background is subtracted from the signal region, yielding the background-subtracted distributions shown in Figure 4.9.

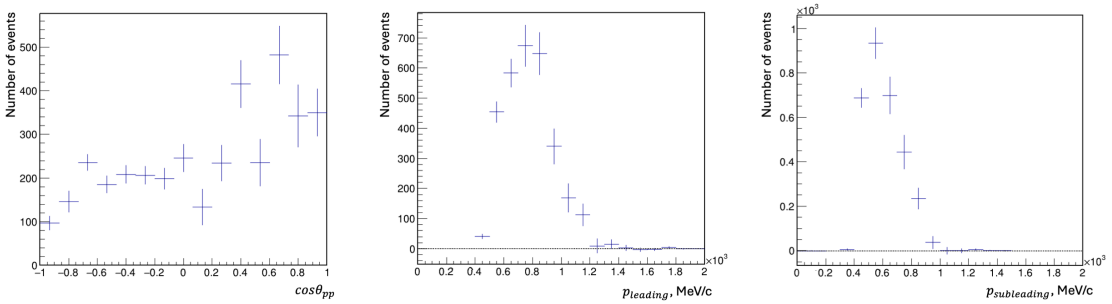

Figure 4.9: Background-subtracted distributions for $\cos(\theta_{pp})$ (left), p_{leading} (middle), and $p_{\text{subleading}}$ (right), obtained after tuning.

4.4 Unfolding

In particle physics experiments, reconstructed event distributions differ from their true distributions due to detector resolution and occasional reconstruction failures. These distortions cause events to migrate between bins, an effect commonly referred to as smearing. To recover the true kinematic distributions from the smeared measurements, an unfolding procedure is applied. This correction is essential for meaningful comparisons with theoretical predictions and other experimental results.

Before applying unfolding, background contributions are subtracted from the reconstructed data. The background-subtracted histograms for each of the three kinematic variables serve as the input to the unfolding process (see Section 4.3.5).

4.4.1 Iterative Bayesian Unfolding

To correct for detector resolution effects, we apply *iterative Bayesian unfolding*, a technique widely used in particle physics to recover true distributions from smeared reconstructed data. This method, introduced by D'Agostini[26], uses Bayes' theorem to iteratively adjust an initial estimate of the true distribution based on the measured data and the detector response.

The unfolding procedure relies on the migration matrix, which encodes the probability that an

event generated in a given true bin is reconstructed in a particular observed bin. Figures 4.10–4.12 show the migration matrices for $\cos(\theta_{pp})$, leading proton momentum, and subleading proton momentum. These matrices represent two-dimensional MC event distributions, illustrating how true events (vertical axis) are reconstructed into measured bins (horizontal axis). Most events lie along the diagonal, with modest off-diagonal migration, indicating that detector resolution is sufficient for these observables and that smearing is moderate.

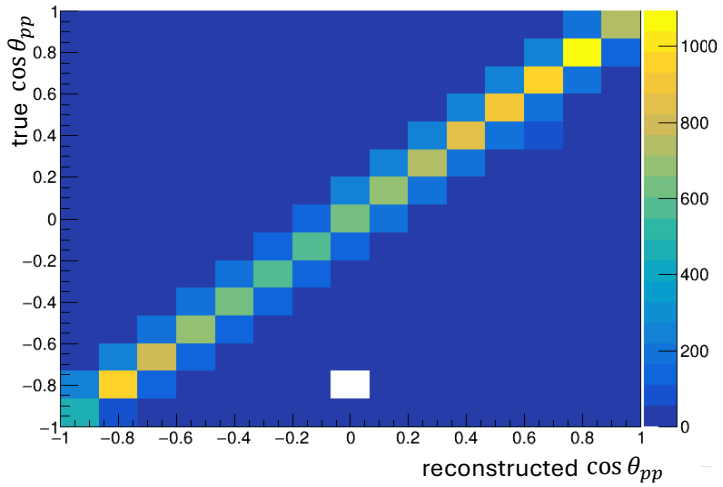

Figure 4.10: Detector response migration matrix for $\cos(\theta_{pp})$ (reconstructed vs. true values). Each element shows the number of events reconstructed in a given observed bin (horizontal) for a true bin (vertical). Off-diagonal elements indicate migration due to finite detector resolution.

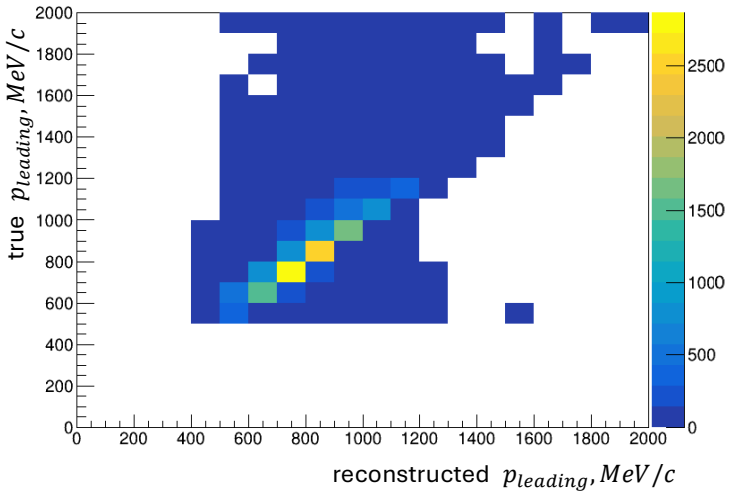

Figure 4.11: Detector response migration matrix for leading proton momentum (reconstructed vs. true values). Most events cluster along the diagonal, demonstrating good reconstruction fidelity.

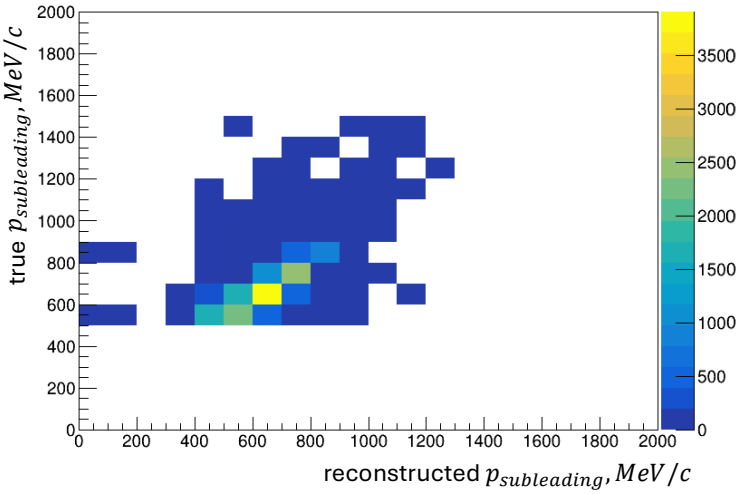

Figure 4.12: Detector response migration matrix for subleading proton momentum (reconstructed vs. true values). Small off-diagonal elements indicate limited smearing.

The algorithm starts with a prior estimate of the true distribution (from MC simulation) and iteratively refines it based on the observed data.

At each iteration:

- The current estimate of the true distribution is *folded* through the migration matrix to predict the reconstructed distribution.
- The prediction is compared to the observed data, and the discrepancy is used to *update* the true distribution estimate.
- This process is repeated until changes in the distribution become small, ensuring stability.

The number of iterations must be chosen carefully: too few iterations leave a possibility of detector effects uncorrected, while too many amplify statistical fluctuations. The optimal number of iterations is determined separately for each analysis variable by monitoring the χ^2 evolution across 100 statistical throws. These statistical throws, also referred to as Poisson throws, are generated by fluctuating the content of each bin in the reconstructed distribution according to Poisson statistics. This simulates the effect of statistical uncertainties that arise from the finite event sample size. By repeating the unfolding process on multiple such fluctuated datasets, we can assess how sensitive the unfolded result is to statistical noise.

For each iteration step, we compute the χ^2 between the reconstructed data and the re-folded unfolded prediction:

$$\chi^2 = \sum_i \frac{(N_i^{\text{data}} - N_i^{\text{refolded}})^2}{\sigma_i^2},$$

where σ_i combines statistical uncertainties from both distributions. This χ^2 should approach the number of degrees of freedom when the unfolding has converged. A plateau near $\chi^2/\text{d.o.f.} \approx 1$ indicates an optimal number of iterations; beyond that point, additional iterations increase statistical variance without improving accuracy.

4.4.2 Application to 2-Proton Analysis

We use the *TransWarpExtraction*[21] tool (MINERvA internal software) to perform iterative Bayesian unfolding for each of the three kinematic variables. This framework allows unfolding to be tested under systematic variations ("warps") to evaluate robustness and model dependence.

Unfolding is inherently model dependent because the migration matrix and the prior distribution are derived from simulation. It is therefore important to confirm that the algorithm remains valid under plausible variations in the interaction model. To probe this, we tested the unfolding across multiple GENIE systematic universes and additional strong linear warps that exaggerate data–MC discrepancies observed in Section 4.2.1.

The GENIE systematic universes considered in this study are:

- **GENIE_MaRES_0 and GENIE_MaRES_1**: These systematics explore variations in the axial mass parameter for resonant pion production. This parameter is crucial in modeling the interaction dynamics where a pion is produced via resonance.
- **GENIE_MFP_pi_0 and GENIE_MFP_pi_1**: These universes investigate the mean free path of pions within the nuclear medium. Understanding the pion interaction length is essential for accurate modeling of pion absorption and scattering processes.
- **GENIE_Theta_Delta2Npi_0 and GENIE_Theta_Delta2Npi_1**: These variations assess the uncertainties in the angular distribution of pions from Delta baryon decays. Accurate angular distributions are critical for reconstructing event kinematics.
- **Low_Recoil_2p2h_Tune_0, Low_Recoil_2p2h_Tune_1, and Low_Recoil_2p2h_Tune_2**: These tunes are designed to improve the modeling of low-recoil events, particularly the 2p2h process. The 2p2h interaction is a complex multi-nucleon process that can significantly affect the observed event rates and kinematics.

To validate the unfolding, for each variable we monitored the χ^2 evolution as a function of iteration count. We generated statistical throws (pseudo-experiments) to check convergence and assessed when the χ^2 stabilizes and becomes comparable to the number of degrees of freedom (d.o.f.), which is the number of unfolded bins.

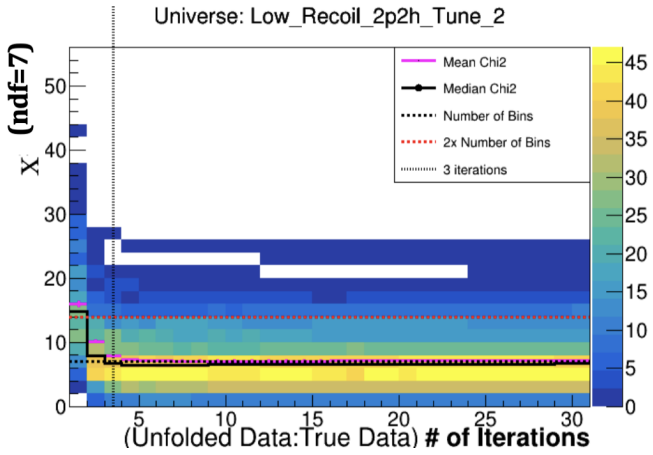

Figure 4.13: Example of chi-square evolution from 1 to 30 iterations with statistical throws for leading proton momentum. The rapid initial drop followed by stabilization indicates that convergence is achieved after approximately three iterations.

As seen in Figure 4.13, where the GENIE systematic universe *Low_Recoil_2p2h_Tune_2* was used to produce a warped distribution of the leading proton momentum, χ^2 settled around the number of degrees of freedom after just three iterations. Similar behavior was observed for other GENIE systematic universes and variables, with *Low_Recoil_2p2h_Tune_2* being one of the strongest warps.

However, since warps based on GENIE systematics alone were not strong enough, as compared to observed significant data-MC discrepancy (4.2.1), we introduced additional strong linear warps to ensure the unfolding method was robust against larger variations. The warping functions applied were:

- For $\cos(\theta_{pp})$: The reconstructed distribution was modified by multiplying by a factor of $(1 + \cos\theta_{pp,true})$.

- For leading and subleading proton momenta: The momentum distributions were warped by a factor of $\left(1 + \frac{p_{true} - 650\ \text{MeV/c}}{300\ \text{MeV/c}}\right)$.

Even under these strong warps, the unfolding procedure successfully brought the χ^2 within the desired range after three iterations for all three variables. This confirms that the chosen unfolding approach is stable and capable of correcting even large distortions in the reconstructed distributions.

Plots illustrating the χ^2 evolution under these linear warps can be seen in Figures 4.14, 4.15, and 4.16.

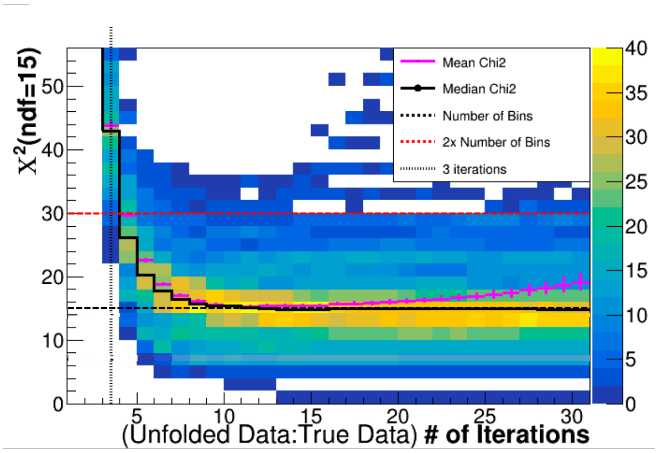

Figure 4.14: χ^2 evolution as a function of unfolding iteration count for $\cos(\theta_{pp})$ after applying a strong linear warp of $1 + \cos\theta_{true}$ across 100 statistical throws.

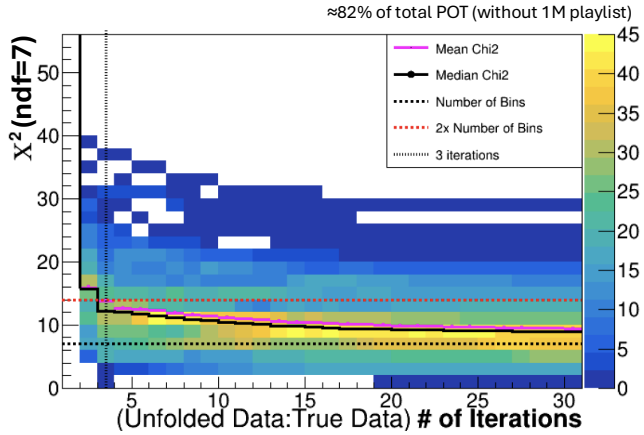

Figure 4.15: χ^2 evolution as a function of unfolding iteration count for leading proton momentum after applying a strong linear warp of $1 + \frac{p_{\text{leading, true}} - 650 \text{ MeV/c}}{300 \text{ MeV/c}}$.

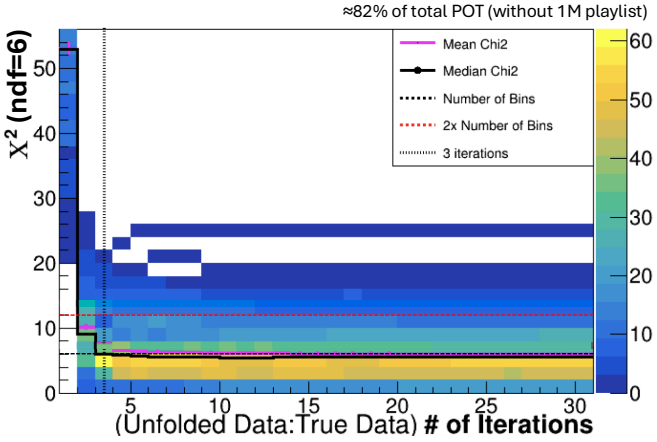

Figure 4.16: χ^2 evolution as a function of unfolding iteration count for subleading proton momentum after applying a strong linear warp of $1 + \frac{p_{\text{subleading, true}} - 650 \text{ MeV/c}}{300 \text{ MeV/c}}$.

4.4.3 Unfolded Results

Based on results of the warping studies above, we chose *three iterations* as the optimal stopping point for all kinematic variables.

Obtained unfolded distributions provide a measurement of the true kinematic spectra corrected for detector resolution effects. As shown in Figures 4.17–4.19, the total uncertainties remain well-controlled across the kinematic range, with statistical contributions dominating over systematic uncertainties in most bins. The impact of different systematic sources varies between observables, but all are within reasonable limits for well-populated bins of respective distributions.

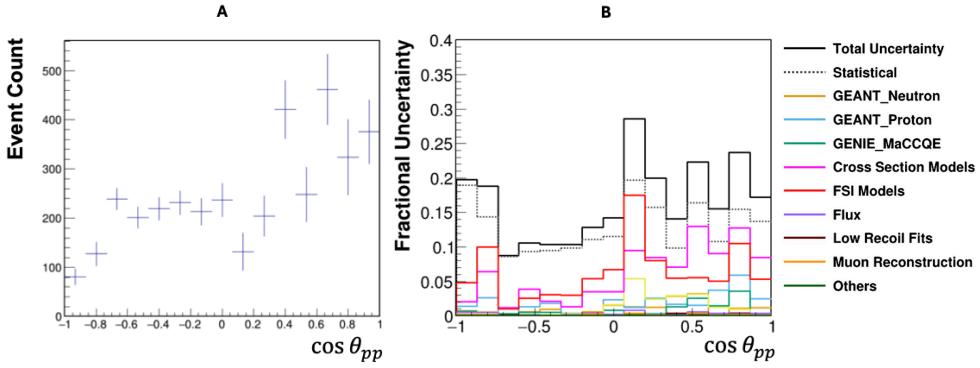

Figure 4.17: (A) Unfolded background-subtracted data distribution of $\cos(\theta_{pp})$. Error bars represent the total uncertainty, including statistical and systematic contributions. (B) Fractional uncertainty breakdown for distribution on the left, showing total uncertainty, as well as contributions from statistical uncertainties, and most significant individual systematic sources.

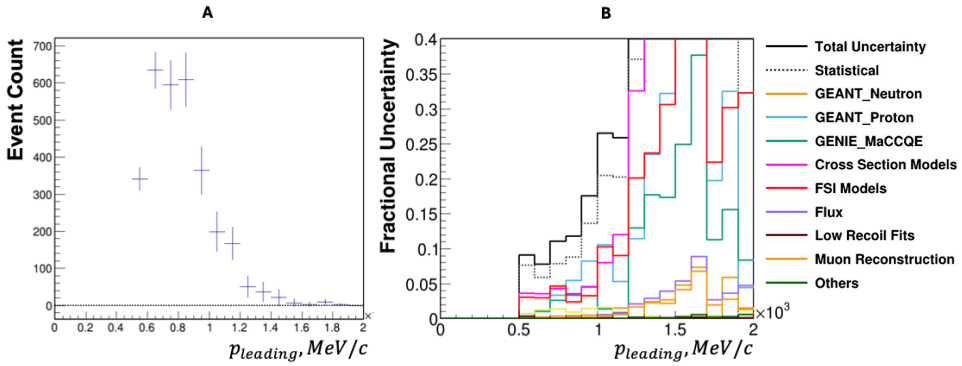

Figure 4.18: (A) Unfolded background-subtracted data distribution of leading proton momentum. Error bars represent the total uncertainty, including statistical and systematic contributions. (B) Fractional uncertainty breakdown for the distribution on the left, showing total uncertainty, as well as contributions from statistical uncertainties and the most significant individual systematic sources.

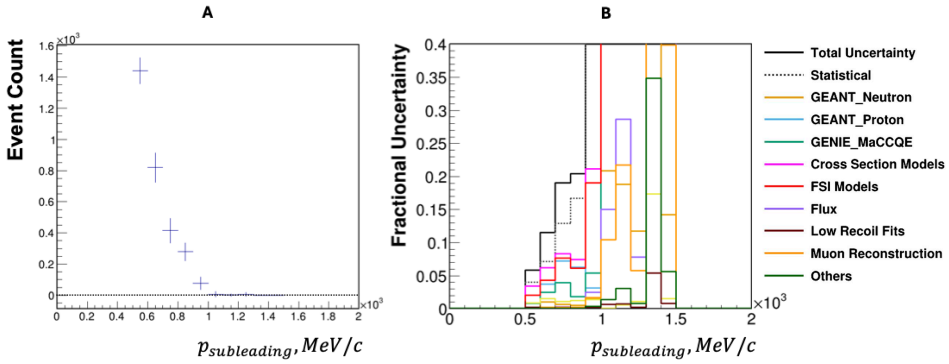

Figure 4.19: (A) Unfolded background-subtracted data distribution of subleading proton momentum. Error bars represent the total uncertainty, including statistical and systematic contributions. (B) Fractional uncertainty breakdown for the distribution on the left, showing total uncertainty, as well as contributions from statistical uncertainties and the most significant individual systematic sources.

To further validate the results, a closure test was performed by refolding the unfolded distributions through the detector response. The agreement between the refolded distributions and the

background-subtracted reconstructed data confirms the stability of the unfolding procedure and its reliability in recovering the true distributions.

The final unfolded histograms serve as the input cross-section extraction, where flux normalization and efficiency corrections will be applied. The consistency across all three variables and the stability of uncertainties indicate that the chosen unfolding procedure effectively accounts for detector smearing while preserving the underlying physics distributions.

4.5 Cross Section Extraction

The final step of the analysis is to extract differential cross-sections by applying efficiency corrections and normalizing to the number of target nucleons and the incident neutrino flux.

The efficiency correction ensures that the measured event rate is properly adjusted for detector acceptance effects. The corrected event distributions are then used to compute the differential cross-sections for the three chosen kinematic variables.

4.5.1 Efficiency Corrections

The efficiency correction ensures that the unfolded signal distributions are properly normalized for detector acceptance and reconstruction effects. The efficiency in each bin i is defined using the Monte Carlo signal sample as:

$$\varepsilon_i = \frac{N_{\text{reco, signal},i}}{N_{\text{true, signal},i}}, \tag{4.3}$$

where:

- $N_{\text{reco, signal},i}$ is the number of reconstructed signal events in bin i;
- $N_{\text{true, signal},i}$ is the number of true signal events in bin i.

These efficiencies, shown in Figures 4.20–4.22, are later applied to the unfolded data distributions (Figures 4.23–4.25).

Cosine of the Angle Between Protons, $\cos(\theta_{pp})$

The efficiency for $\cos(\theta_{pp})$ is relatively flat across most of the angular range, remaining around 6-7% for $\cos(\theta_{pp}) < 0$ and gradually increasing to about 8-9% for $\cos(\theta_{pp}) > 0$ (Figure 4.20). The first and last bins have noticeably lower efficiency, reflecting reduced acceptance for highly back-to-back ($\cos\theta_{pp} \approx -1$) and strongly forward ($\cos\theta_{pp} \approx +1$) configurations. In these extreme regions, one or both protons are more likely to exit the detector volume or produce tracks that fail containment and reconstruction-quality criteria, leading to lower selection efficiency.

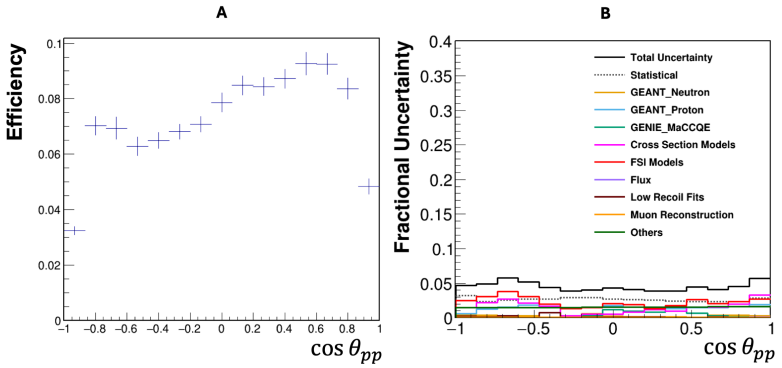

Figure 4.20: (A) Efficiency as a function of $\cos(\theta_{pp})$. (B) Fractional uncertainties for the efficiency.

Leading Proton Momentum, p_{leading}

The efficiency for leading proton momentum increases rapidly from 0.5 GeV/c until it peaks around 0.8–0.9 GeV/c, then decreases at higher momenta (Figure 4.21). The rise at low momentum corresponds to the transition from short, poorly reconstructed tracks to fully contained, well-measured protons. Efficiency peaks near 0.8–0.9 GeV/c, where protons typically stop within the tracker and exhibit clear Bragg-like energy-deposition patterns. At higher momenta, efficiency de-

creases because such protons are less likely to stop elastically: their dE/dx profiles no longer show the characteristic rise toward a Bragg peak, causing them to fail the ESC (Elastically Scattering Contained) selection (see 4.2).

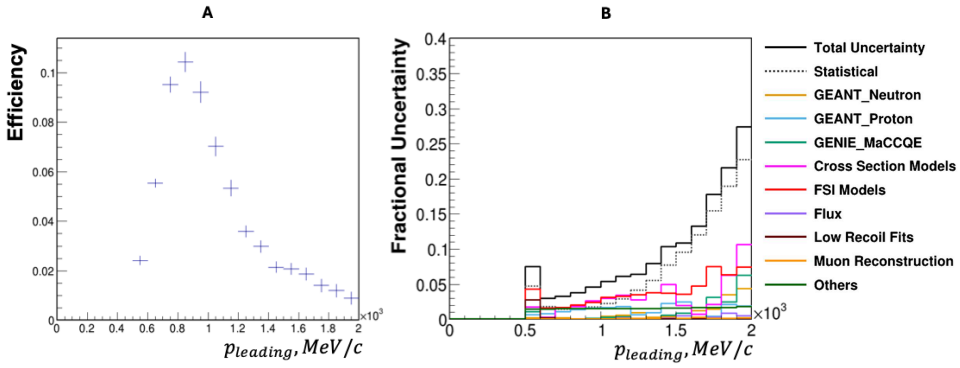

Figure 4.21: (A) Efficiency as a function of leading proton momentum. (B) Fractional uncertainties for the efficiency.

Subleading Proton Momentum, $p_{\text{subleading}}$

The subleading-proton efficiency follows a similar trend but decreases more steeply beyond its peak near 0.8 GeV/c (Figure 4.22). This stronger falloff occurs because events with a high-momentum subleading proton typically have an even more energetic leading proton, making both less likely to satisfy the ESC containment requirement.

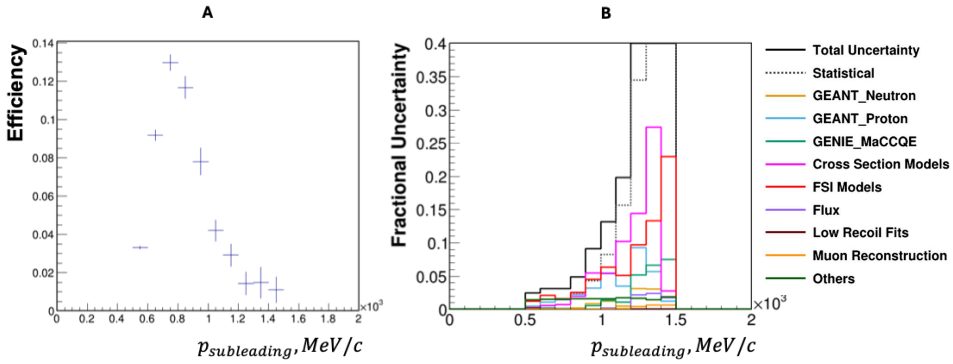

Figure 4.22: (A) Efficiency as a function of subleading proton momentum. (B) Fractional uncertainties for the efficiency.

4.5.2 Efficiency-Corrected Distributions

After applying efficiency corrections, we obtain the efficiency-corrected distributions, which serve as inputs to the final cross-section calculation.

Cosine of the Angle Between Protons, $\cos(\theta_{pp})$

The efficiency-corrected distribution has a U-shape, rising towards $\cos(\theta_{pp}) \approx -1$ and $+1$, with the lowest values near $\cos(\theta_{pp}) \approx 0$ (Figure 4.23).

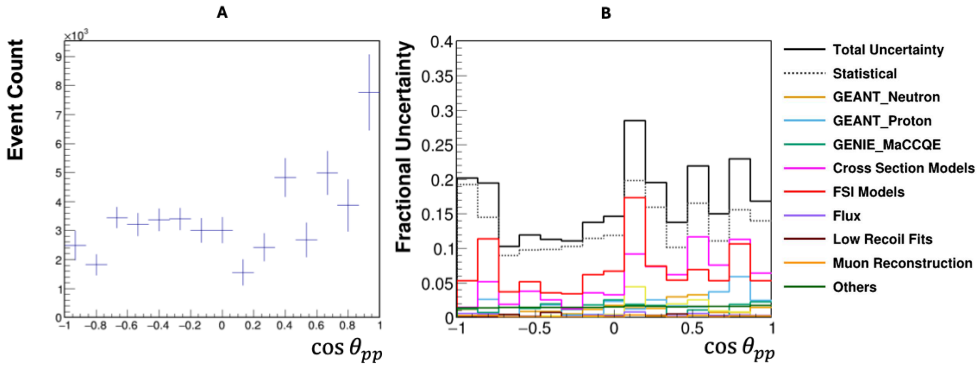

Figure 4.23: (A) Efficiency-corrected distribution of $\cos(\theta_{pp})$. (B) Fractional uncertainties for the efficiency-corrected distribution.

Leading Proton Momentum, p_{leading}

The efficiency-corrected distribution of p_{leading} shows a sharp decline for larger momenta, rapidly approaching the horizontal axis (Figure 4.24).

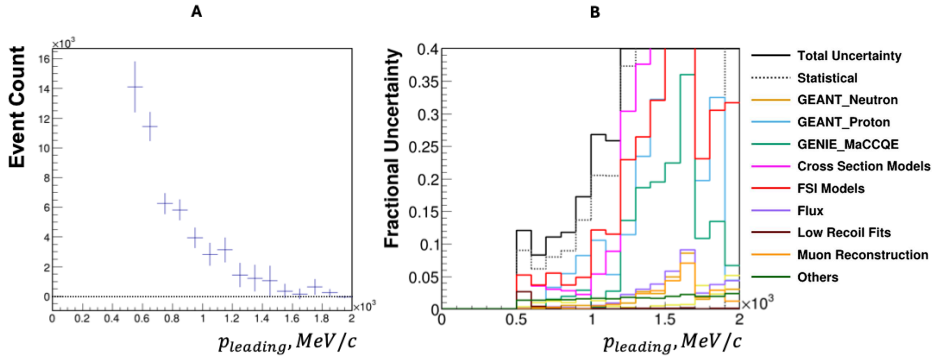

Figure 4.24: (A) Efficiency-corrected distribution of leading proton momentum. The shape decreases sharply beyond 0.5 GeV/c. (B) Fractional uncertainties for the efficinecy-corrected distribution.

Subleading Proton Momentum, $p_{\text{subleading}}$

The subleading proton momentum distribution follows a trend similar to the leading proton momentum but has a steeper decline after the first populated bin (Figure 4.25).

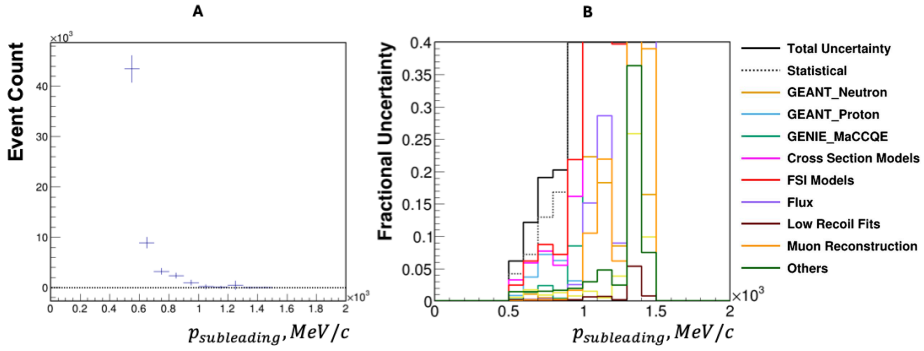

Figure 4.25: (A) Efficiency-corrected distribution of subleading proton momentum. (B) Fractional uncertainties for the efficiency-corrected distribution.

4.5.3 Final Differential Cross-Sections

The final cross-section is obtained by normalizing the efficiency-corrected event rate to the flux and number of target nucleons.

$$\frac{d\sigma}{dX} = \frac{N_{\text{corrected}}}{\Phi T \Delta X} \tag{4.4}$$

where: $N_{\text{corrected}}$ is the efficiency-corrected distribution, Φ is the total integrated neutrino flux, T is the number of target nucleons in the fiducial volume, ΔX is the bin width.

Although the two-proton topology originates from nuclear (multi-nucleon) processes, normalization per target nucleon is used following MINERvA convention to facilitate comparison with other measurements.

The resulting differential cross sections are shown in Figures 4.26–4.28. Negative values at the

plot edges arise only from error bars in bins with small event counts; a dotted horizontal line at zero is drawn for reference where applicable.

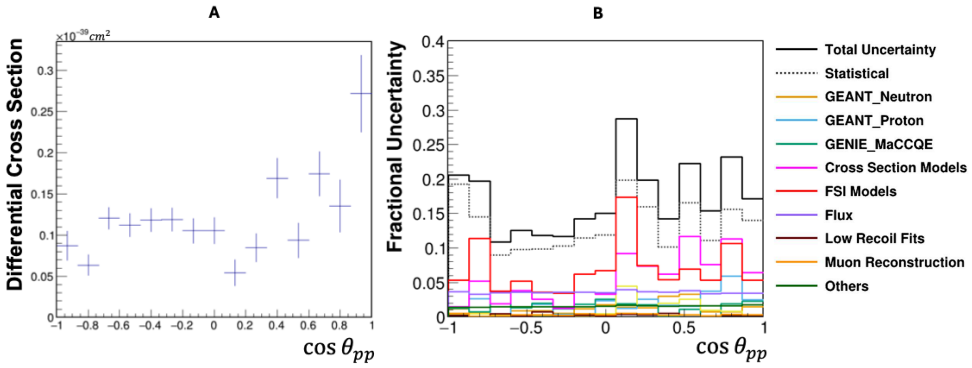

Figure 4.26: (A) Differential cross-section for $\cos(\theta_{pp})$. (B) Fractional uncertainty contributions. Statistical uncertainties dominate, while systematics from cross-section models and detector effects are largest.

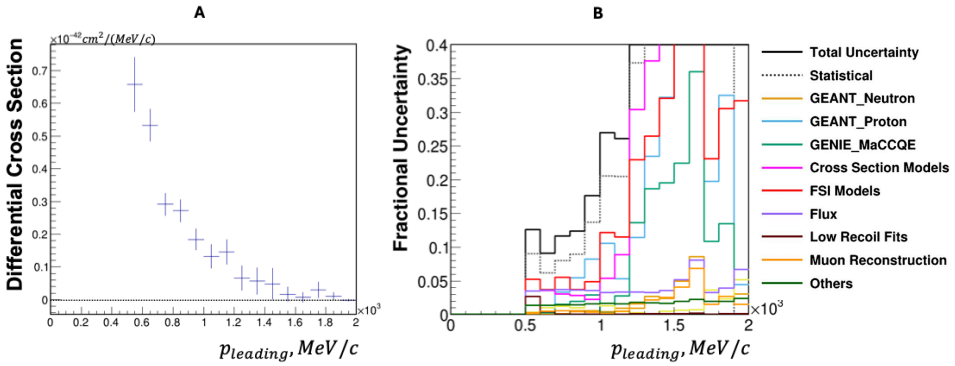

Figure 4.27: (A) Differential cross-section for leading proton momentum. (B) Fractional uncertainty contributions. Statistical uncertainties dominate in well-populated bins, while systematics from cross-section models and detector effects are largest.

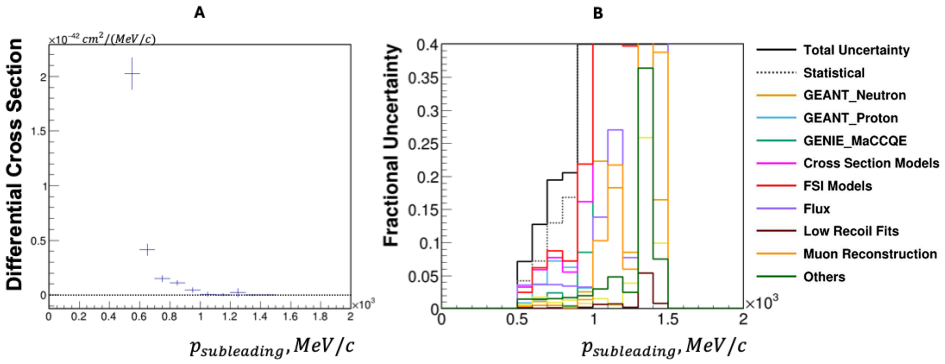

Figure 4.28: (A) Differential cross-section for subleading proton momentum. (B) Fractional uncertainty contributions. Statistical uncertainties dominate in well-populated bins, while systematics from cross-section models and detector effects are largest.

Science is the poetry of reality.

Vladimir Vernadsky

5

Conclusions

This thesis has presented a measurement of muon–neutrino charged–current (ν_μ CC) interactions producing two protons and no pions in the final state, using the MINERvA detector exposed to the NuMI beam at Fermilab. These rare, exclusive topologies provide a sensitive probe of nuclear effects in neutrino interactions—specifically the interplay between quasielastic (QE) dynamics, multinucleon correlations (2p2h), and final–state interactions (FSI). They also test the predictive power of neutrino event generators, which play a central role in oscillation analyses for current and

future long-baseline experiments.

5.1 Summary of Results

The analysis reported single-differential cross sections as functions of three key kinematic variables:

1. the cosine of the opening angle between the two protons, $\cos(\theta_{pp})$,
2. the momentum of the leading proton,
3. the momentum of the subleading proton.

These results were obtained after careful event selection, background tuning with sideband samples, iterative Bayesian unfolding, and efficiency corrections. The extracted cross sections represent the first MINERvA measurement of two-proton final states in ν_μ CC interactions. Comparisons to simulation use GENIE v2.12 with the MINERvA Tune v2 as the baseline model.

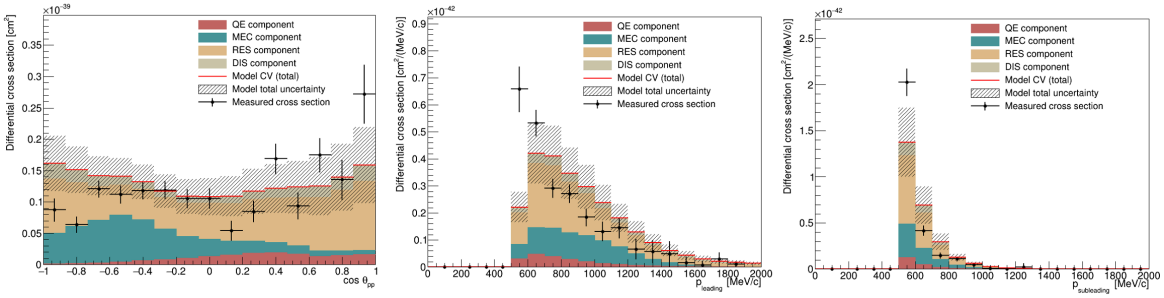

Figure 5.1: Comparison between the measured and simulated differential cross sections for the three analyzed observables. **Left:** $\cos(\theta_{pp})$ distribution. **Middle:** Leading-proton momentum distribution. **Right:** Subleading-proton momentum distribution. The simulated prediction is shown decomposed by interaction type—quasielastic (QE), multinucleon (MEC/2p2h), resonance (RES), and deep-inelastic scattering (DIS).

Shape of Angular Distribution

The measured $\cos(\theta_{pp})$ distribution does not exhibit the pronounced U-shape seen in the simulation (Fig. 5.1). In GENIE the true cross section peaks near both back-to-back ($\cos\theta_{pp} \approx -1$) and

collinear ($\cos\theta_{pp} \approx +1$) configurations, reflecting multinucleon and FSI dynamics. In contrast, the data show a smoother pattern: near $\cos\theta_{pp} \approx 0$ measurement and simulation agree closely, while for $\cos\theta_{pp} > 0$ the data fluctuate about the model without a clear trend. For $\cos\theta_{pp} < 0$, the measured cross section consistently trails below the prediction, becoming significantly smaller near $\cos\theta_{pp} \simeq -1$. This suggests that GENIE may overpredict strongly back-to-back configurations, possibly due to excessive pion-absorption strength or insufficient proton attenuation in the nucleus. Smooth sideband shapes (Fig. 4.4) argue against a detector- or background-model artifact. Truth-level study (Fig. 5.2), as well as the behavior of components to GENIE prediction (Fig. 5.1) show how different interaction modes populate angular regions and motivate targeted generator tests.

	QEL	MEC	RES	DIS	Σ
All events	239,082	71,914	422,993	791120	1,599,875
+0-π	226,058	70,783	71,032	36,165	404,038
+μ-cuts	214,201	67,617	66,991	32,168	392,977
+$MultiP$	54,207	56,819	54,159	16,321	181,506
+p-cuts	2,148	6,769	15,621	4,863	29,401

Figure 5.2: Table with counts of events passing cuts from one of the early truth studies. From MINERvA doc-26674.

Proton–momentum spectra and momentum sharing

Both leading- and subleading-proton cross sections fall more steeply with momentum in data than in GENIE (Fig. 5.1), i.e., the data prefer a softer proton spectrum. Three (non-exclusive) mechanisms can drive this:

- **2p2h momentum sharing:** If the model assigns too large a share of the available energy *after nuclear removal energy* to one nucleon, or generically produces harder nucleon spectra, it will overpopulate the high-p tails.

- **FSI energy loss:** An intranuclear cascade that is too transparent (insufficient energy loss and rescattering) also yields protons that are too hard.

- **Pion-absorption mix:** The relative rate/kinematics of π production followed by intranuclear absorption influences both $\cos\theta_{pp}$ and proton p; mismodeling this balance can harden the spectra.

- **Removal (separation) and missing excitation energy:** If the energy required to liberate nucleons and excite the residual nucleus is underestimated, too much kinetic energy is left for the outgoing protons (hardening the spectra); overestimation would soften them.

What we can conclude is that the hadronic system in data emerges with less proton kinetic energy than GENIE predicts. What we cannot yet isolate is *which* of the above mechanisms dominates: our current observables are hadron-only, so even if the *magnitude of the three-momentum transfer* $|\vec{q}|$ (constrained by the muon) is modeled reasonably on average, the *partition* of hadronic energy among protons, neutrons, nuclear removal/excitation, and unobserved channels can still differ and produce the observed softening. The 2D hadron–lepton observables proposed in Sec. 5.5 (e.g. $d^2\sigma/d(\cos\theta_{pp})\,dp_T^{\mu}$) are designed to break this degeneracy.

Background Modeling

The sideband–based background tuning procedure successfully constrained charged- and neutral-pion contamination (Fig. 4.6).

This tuning reduced the dependence on GENIE's underlying pion-production model and improved confidence in the extracted signal distributions.

A principal goal was to understand the balance of mechanisms that yield two-proton, no-pion final states: (1) genuine two-particle–two-hole (2p2h/MEC) interactions driven by two-body nuclear currents, and (2) pion production followed by intranuclear π absorption (an FSI process).

Two-Particle–Two-Hole Processes

2p2h interactions arise from two-body nuclear currents, including short-range correlations and meson-exchange currents. Figure 5.3 schematically illustrates the kinematics in the hadronic rest frame.

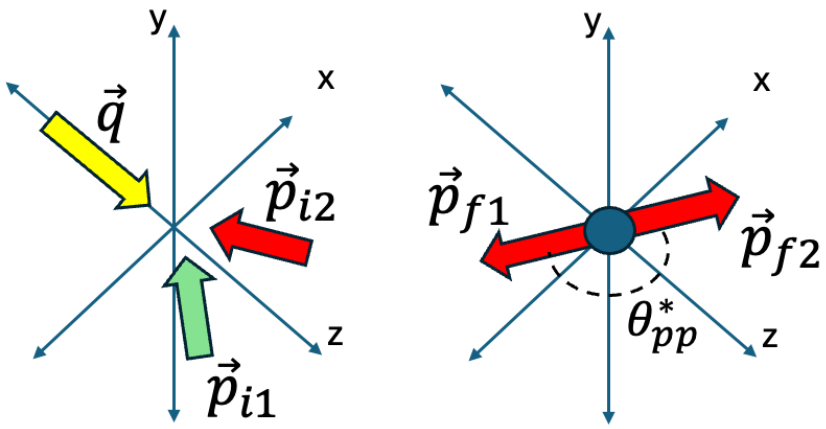

Figure 5.3: Two-particle two-hole interaction in the hadronic rest frame. The initial state is shown on the left, the final state on the right. The momentum transfer is indicated in yellow, protons in red, and neutrons in green. The angle θ^*_{pp} represents the separation between the two final-state protons in this frame.

In this frame, scattering from a correlated neutron–proton pair produces nearly back-to-back protons; in the laboratory frame, boosts and rescattering modify this angle. Most generators, including GENIE, employ the simplest possible approach and generate an isotropic distribution in this

frame[60].

One expectation from nuclear theory is that scattering predominantly occurs from deuteron-like neutron–proton (*np*) pairs inside the nucleus, which possess large relative momentum but small total momentum[56]. Electron-scattering measurements confirm that two-nucleon knockout is dominated by such *np* short-range–correlated (SRC) pairs, with only about 6% arising from proton–proton pairs[27]. Because neutrinos interact primarily with neutrons, only those 2p2h interactions that strike the neutron in an *np* pair lead to two outgoing protons—one produced at the neutrino–neutron vertex and the other ejected as its correlated partner.

Theoretical cross sections are calculated from contractions of lepton and hadron tensors[57], using tabulated hadron tensors derived from effective nuclear models. While this formalism facilitates implementation and reweighting, it limits the ability to propagate theory uncertainties and requires an independent prescription for the outgoing-nucleon kinematics.

Pion Absorption and Final-State Interactions

Pion absorption following an inelastic 1p1h interaction (Fig. 5.4) can mimic a two-proton topology. These events originate from resonant pion production with subsequent π absorption inside the nucleus.

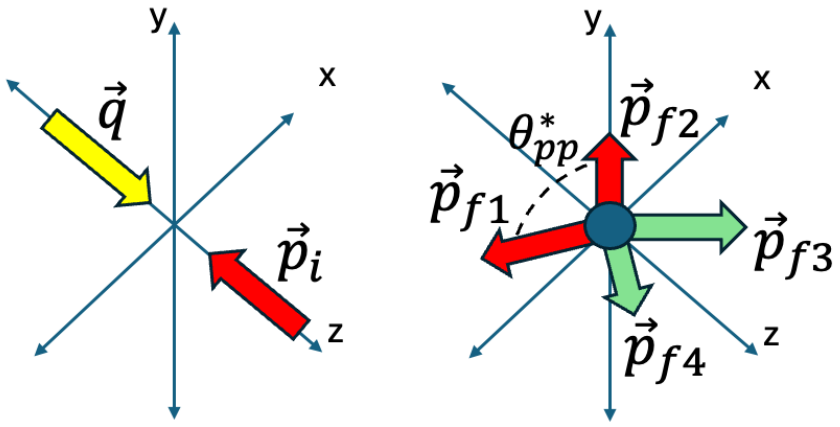

Figure 5.4: Pion absorption in the hadronic rest frame. Initial state is on the left, final state on the right. The momentum transfer is shown in yellow, protons are red, and neutrons are green. The angle θ^*_{pp} is the angle between the two final state protons in the hadronic rest frame. This schematic omits the intermediate pion and depicts only the final state after intranuclear absorption.

In GENIE, such processes are handled through the intranuclear cascade model. Our sideband constraints show that this background remains non-negligible but is well controlled after tuning.

Our comparison suggests that the generator's composition and/or kinematics of these channels are not yet optimal: data disfavor the most strongly back-to-back topologies, and both proton spectra are softer than predicted.

5.3 Uncertainties and their behavior

We report both statistical and systematic uncertainties, including flux, cross-section model, intranuclear FSI, and detector/GEANT components. A notable feature is the jitter seen in some bins of the fractional uncertainty (Fig. 4.26). This has a straightforward origin:

- In bins where the **signal yield is small** and the **background is sizeable**, the tuned background subtraction is large, so the **denominator** of the fractional uncertainty (the unfolded,

efficiency-corrected signal) is small.

- At the same time, **background uncertainties** (and their correlations), **migration effects** near thresholds, and **efficiency variations** are comparatively large.

The combination of a large subtraction and a small denominator produces elevated fractional uncertainties and bin-to-bin structure. This is expected behavior and aligns with where selection efficiency falls, migrations are strongest, and sideband constraints carry the most weight

5.4 Comparison to Other Measurements

ArgoNeuT [5] first identified "hammer-like" two-proton events in LAr, and MicroBooNE [3] measured a broader 2p2h-enhanced sample with significant model spread. Relative to those LArTPC results, this measurement provides the first cross sections on a hydrocarbon target at higher average energy.

An important kinematic mapping between experiments is the **boost of the momentum-transfer system**. MINERvA's higher typical neutrino energies and Q^2 push the hadronic system more forward than in MicroBooNE's BNB conditions, which can naturally modify the observed $\cos\theta_{pp}$ shape. Thus, part of the MINERvA–MicroBooNE difference may be attributable to frame/boost effects, not solely to model mismodeling. This underlines the value of comparable observables (including joint lepton–hadron variables) across targets and energy regimes.

Other MINERvA measurements emphasizing 2p2h-sensitive observables, such as the transverse-kinematic-imbalance (TKI) analyses [53], also show data–model shape tensions, reinforcing that multinucleon and FSI implementations in generators require refinement.

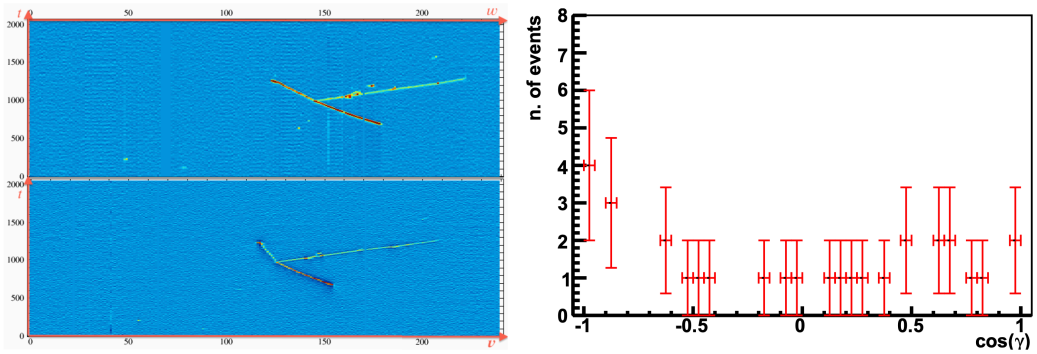

Figure 5.5: Results from the ArgoNeuT two-proton ("hammer") analysis[5]. **Left:** Event display of a characteristic hammer-like topology in the ArgoNeuT liquid-argon time projection chamber (LArTPC), showing two reconstructed proton tracks back-to-back with respect to the muon direction. **Right:** Distribution of the cosine of the angle between the two protons, $\cos(\gamma)$, for the selected sample of 30 events. The concentration of events near $\cos(\gamma) \approx -1$ indicates a strong back-to-back correlation consistent with scattering from short-range correlated np pairs in the nucleus. This pioneering measurement established the experimental feasibility of identifying correlated two-proton final states in LArTPC detectors.

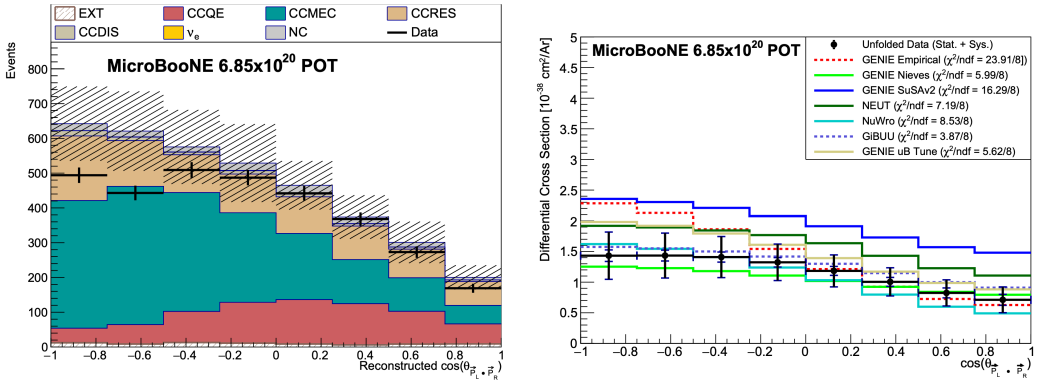

Figure 5.6: Results from the MicroBooNE measurement of two-proton (2p2h-enhanced) muon–neutrino interactions[3]. **Left:** Reconstructed distribution of $\cos(\theta_{pp})$. Data points are shown together with the simulated prediction, which is divided into contributions from quasielastic scattering, resonant pion production, multinucleon (2p2h/MEC) interactions, deep-inelastic scattering, neutral-current and electron-neutrino events, and a small beam-off (cosmic) background component. **Right:** Differential cross section as a function of $\cos(\theta_{pp})$, comparing the unfolded MicroBooNE data with several theoretical and generator predictions: GENIE (Empirical and Nieves implementations), SuSAv2, NEUT, NuWro, GiBUU, and the tuned GENIE "uB-Tune." The spread among model curves illustrates the current theoretical uncertainty in describing multinucleon and FSI dynamics, while the data provide an important benchmark for model validation.

5.5 Future Work

For MINERvA

This analysis is the first in MINERvA to isolate two-proton, no-pion final states, so it was intentionally limited to three one-dimensional observables to establish a baseline measurement. Its natural extensions are:

- **Double-differential cross sections** such as $d^2\sigma/d(\cos\theta_{pp})\,dp$ and $d^2\sigma/dp_{\text{leading}}\,dp_{\text{subleading}}$ to disentangle angular–momentum correlations.
- **Joint lepton–hadron observables**, e.g. $d^2\sigma/d(\cos\theta_{pp})\,dp_T^{\mu}$, to relate momentum sharing directly to the momentum transfer.
- **Transverse kinematic imbalance (TKI) variables** (Δp_T, $\delta\alpha_T$, $\delta\varphi_T$), which are sensitive to Fermi motion and FSI effects and can be directly compared with previous MINERvA TKI measurements[53].
- **Hadronic rest-frame studies** of θ^*_{pp} to test the isotropic emission assumption.
- **Extended topologies**, e.g. three-proton events or neutron activity, to separate 2p2h from π absorption with higher purity.

A complementary variable is the lepton-plane hemisphere asymmetry, defined as $A_{\text{hemi}} = 0$ when both protons lie in the same hemisphere relative to the lepton scattering plane and $A_{\text{hemi}} = 1$ when they are in opposite hemispheres. This asymmetry provides a compact, detector-robust probe of angular correlations between the two protons.

For Theory and Generators

The results presented here provide new constraints on how event generators model the balance between 2p2h and pion-absorption processes and how momentum is shared between outgoing nucleons. A distinctive strength of this measurement is its focus on the hadronic system: while most 2p2h calculations are validated using lepton kinematics, this analysis probes the nucleon side directly. Because generator implementations predict both lepton and hadron observables through the same underlying contraction of lepton and hadron tensors, the two-proton results presented here offer a unique handle on the hadronic component of the model—particularly on how the available energy, less the nuclear removal energy, is partitioned between the two ejected nucleons. At the same time, our data alone do not uniquely determine momentum sharing: a steeper proton spectrum in data can also arise from final-state interactions or from the back-to-back component of pion absorption; joint lepton–hadron observables are needed to break these degeneracies.

These findings motivate several theoretical and generator developments:

- **Two-nucleon kinematics:** Implement anisotropic emission models consistent with scattering from deuteronlike np pairs, as suggested by electron-scattering data, to improve the description of $\cos\theta_{pp}$ and momentum correlations. Validate such models across flux/energy regimes by folding predictions to both MINERvA (NuMI ME) and MicroBooNE (BNB) conditions to separate intrinsic model effects from frame/boost ($|\vec{q}|$, Q^2) differences that can reshape $\cos\theta_{pp}$.

- **Final-state interactions:** The observed suppression at negative $\cos\theta_{pp}$ and the steeper fall of the proton-momentum spectra in data indicate that intranuclear cascade parameters (mean free paths, charge exchange, absorption) should be retuned using proton-based observables. In particular, test whether the back-to-back component from π absorption is overpredicted in the current cascade.

- **Systematic parameterization:** For oscillation analyses, 2p2h and FSI effects should be represented through a small set of orthogonal "dials" controlling normalization, energy dependence, nucleon-pair composition, and angular anisotropy. The approach developed for DUNE [19] provides a framework for propagating these uncertainties consistently.
- **Cross-framework validation:** Direct comparisons between GENIE, NuWro, and GiBUU using identical phase-space and detector conditions would isolate true model differences and identify the most robust hadronic predictions.

For Future Experiments

The findings have immediate relevance for current and next-generation oscillation programs:

- **NOvA and T2K:** The two-proton results inform cross-section systematics that impact hadronic energy reconstruction and lepton–hadron kinematic correlations used in energy estimators.
- **DUNE:** These hydrocarbon-based measurements provide complementary constraints for tuning argon-target simulations in the multi-GeV regime, where 2p2h and FSI uncertainties are among the largest [19]. The DUNE ND-LAr detector can apply the same $\cos\theta_{pp}$, momentum, and TKI observables at high statistics to validate generator models across targets.
- **Liquid-argon detectors (SBN, ND-LAr):** The results emphasize the importance of multi-proton reconstruction with precise angular resolution and neutron tagging. Consistent analyses on carbon and argon targets will allow direct tests of nuclear dependence in multinucleon dynamics.

A comprehensive multi-model comparison, as well as the proposed additional observables, are natural pathways for future analyses. They are minimally dependent on detector-specific effects and

provide high sensitivity to the distinct nuclear processes underlying two-proton final states.

5.6 Concluding Remarks

This work demonstrates that precision measurements of exclusive two-proton, no-pion final states are feasible in a segmented scintillator detector such as MINERvA. By isolating and unfolding a clean sample, this analysis provides new empirical constraints on multinucleon dynamics and intranuclear rescattering. The results bridge inclusive cross-section measurements and the fully reconstructed topologies accessible to modern LArTPC detectors. They contribute to the global effort to reduce neutrino-interaction uncertainties and thereby enhance the precision of neutrino-oscillation physics.

References

[1] Aartsen, M. G. et al. 2021, 'IceCube-Gen2: the window to the extreme Universe', *J. Phys. G* **48**(6), 060501.

[2] Abe, K. et al. 2018, 'Hyper-Kamiokande Design Report'.

[3] Abratenko, P. et al. 2022, 'First Measurement of Differential Cross Sections for Muon Neutrino Charged Current Interactions on Argon with a Two-proton Final State in the MicroBooNE Detector'.

[4] Abubakar, S. et al. 2025, 'Precision measurement of neutrino oscillation parameters with 10 years of data from the NOvA experiment'.

[5] Acciarri, R. et al. 2014*a*, 'Detection of Back-to-Back Proton Pairs in Charged-Current Neutrino Interactions with the ArgoNeuT Detector in the NuMI Low Energy Beam Line', *Phys. Rev. D* **90**(1), 012008.

[6] Acciarri, R. et al. 2014*b*, 'Measurements of Inclusive Muon Neutrino and Antineutrino Charged Current Differential Cross Sections on Argon in the NuMI Antineutrino Beam', *Phys. Rev. D* **89**(11), 112003.

[7] Acciarri, R. et al. 2015, 'Long-Baseline Neutrino Facility (LBNF) and Deep Underground Neutrino Experiment (DUNE): Conceptual Design Report, Volume 2: The Physics Program for DUNE at LBNF'.

[8] Acciarri, R. et al. 2016, 'Long-baseline neutrino facility (lbnf) and deep underground neutrino experiment (dune) conceptual design report volume 1: The lbnf and dune projects'.

URL: *https://arxiv.org/abs/1601.05471*

[9] Acero, M. A. et al. 2016, 'Observation of electron neutrino appearance in muon neutrino beam', *Phys. Rev. Lett.* **116**, 151806.

[10] Adamson, P. et al. 2016, 'The NuMI Neutrino Beam', *Nucl. Instrum. Meth. A* **806**, 279–306.

[11] Adamson, P. et al. 2020, 'Precision constraints for three-flavor neutrino oscillations from the full minos and minos+ dataset', *Phys. Rev. Lett.* **125**(13), 131802.

[12] Agostinelli, S. et al. 2003, 'GEANT4: A Simulation toolkit', *Nucl. Instrum. Meth. A* **506**, 250–303.

[13] Aliaga, L. et al. 2014, 'Design, calibration, and performance of the minerva detector', *Nucl. Instrum. Meth. A* **743**, 130–159.

[14] Aliaga, L. and et al. (MINERvA Collaboration) 2015, 'Minerva neutrino detector response measured with test beam data', *Nuclear Instruments and Methods in Physics Research Section A* **789**, 28–42.

URL: *https://arxiv.org/abs/1501.06431*

[15] Aliaga Soplin, L. 2016, Neutrino Flux Prediction for the NuMI Beamline, PhD thesis, William-Mary Coll.

[16] Allison, T. A. et al. 2017, 'The GENIE Neutrino Monte Carlo Generator: Physics and User Manual', *Nucl. Instrum. Meth. A* **859**, 106–133.

[17] Altinok, O. et al. 2017, 'Measurement of ν_μ Charged-Current Single π^0 Production on Hydrocarbon in the Few-GeV Region Using MINERvA', *Phys. Rev. D* **96**(7), 072003.

[18] An, F. et al. 2016, 'Neutrino Physics with JUNO', *J. Phys. G* **43**(3), 030401.

[19] Bathe-Peters, L. 2025, '2p2h cross-section systematics in dune'. arXiv preprint, to appear in the DUNE Physics Working Group documentation.

URL: *https://arxiv.org/abs/2501.08725*

[20] Benhar, O., Farina, N., Nakamura, H., Sakuda, M. and Seki, R. 2005, 'Electron- and neutrino-nucleus scattering in the impulse approximation regime', *Phys. Rev. D* **72**, 053005.

[21] Bercellie A., R. D. 2018, Transwarpextraction tool instructions, Technical Report MINERvA DocDB 18488-v3, Fermilab. Internal document.

URL: *https://minerva-docdb.fnal.gov/cgi-bin/sso/ShowDocument?docid=18488*

[22] Cahn, R. N., Dwyer, D. A., Freedman, S. J., Haxton, W. C., Kadel, R. W., Kolomensky, Y. G., Luk, K. B., McDonald, P., Gann, G. D. O. and Poon, A. W. P. 2013, 'White paper: Measuring the neutrino mass hierarchy'.

URL: *https://arxiv.org/abs/1307.5487*

[23] Cleveland, B. T., Daily, T., Davis, Jr., R., Distel, J. R., Lande, K., Lee, C. K., Wildenhain, P. S. and Ullman, J. 1998, 'Measurement of the solar electron neutrino flux with the homestake chlorine detector', *The Astrophysical Journal* **496**(1), 505.

URL: *https://dx.doi.org/10.1086/305343*

[24] Collaboration, M., Aliaga, L., Altinok, O., Castillo, C. A. D., Bagby, L., Bellantoni, L., Bergan, W. F., Bodek, A., Bradford, R., Bravar, A., Budd, H., Butkevich, A., Caicedo, D. A. M., Carneiro, M. F., Christy, M. E., Chvojka, J., da Motta, H., Devan, J., Diaz, G. A., Dytman, S. A., Eberly, B., Felix, J., Fields, L., Fine, R., Flight, R., Gago, A. M., Gingu, C., Golan, T., Gomez, A., Gran, R., Harris, D. A., Higuera, A., Howley, I. J., Hurtado, K., Kleykamp, J., Kordosky, M., Lanari, M., Le, T., Leister, A. J., Lovlein, A., Maher, E., Mann, W. A., Marshall, C. M., McFarland, K. S., McGivern, C. L., McGowan, A. M., Messerly, B., Miller, J., Miller, W., Mislivec, A., Morfin, J. G., Mousseau, J., Muhlbeier, T., Naples, D., Nelson, J. K., Norrick, A., Ochoa, N., OConnor, C. D., Osmanov, B., Osta, J., Paolone, V., Patrick, C. E., Patrick, L., Perdue, G. N., Lara, C. E. P., Rakotondravohitra, L., Ramirez, M. A., Ray, H., Ren, L., Rodrigues, P. A., Rubinov, P., Rude, C. R., Ruterbories, D., Schellman, H., Schmitz, D. W., Salinas, C. J. S., Tagg, N., Tice, B. G., Urrutia, Z., Valencia, E., Walton, T., Westerberg, A., Wolcott, J., Woodward, N., Wospakrik, M., Zavala, G., Zhang, D. and Ziemer, B. P. 2015, 'Minerva neutrino detector response measured with test beam data'.

URL: *https://arxiv.org/abs/1501.06431*

[25] Cush 2018, 'Standard model of elementary particles', Wikimedia Commons. Public domain image, accessed 2025-09-23.

URL: *https://commons.wikimedia.org/wiki/File:Standard_Model_of_Elementary_Particles_Anti.svg*

[26] D'Agostini, G. 1995, 'A multidimensional unfolding method based on bayes' theorem', *Nuclear Instruments and Methods in Physics Research Section A: Accelerators, Spectrometers, Detectors and Associated Equipment* **362**(2), 487–498.

URL: *https://www.sciencedirect.com/science/article/pii/016890029500274X*

[27] Duer, M. et al. 2019, 'Direct Observation of Proton-Neutron Short-Range Correlation Dominance in Heavy Nuclei', *Phys. Rev. Lett.* **122**(17), 172502.

[28] Dytman, S. 2011, Final state interaction models in neutrino-nucleus scattering, *in* 'AIP Conf. Proc.', Vol. 1405, pp. 213–218.

[29] Eigen, M. 1971, 'Selforganization of matter and the evolution of biological macromolecules', *Naturwissenschaften* **58**(10), 465–523.

[30] Feynman, R. P. 1969, 'Very high-energy collisions of hadrons', *Phys. Rev. Lett.* **23**, 1415–1417.

[31] Fields, L. et al. 2013, 'Measurement of Neutrino and Antineutrino Quasielastic-like Scattering on Hydrocarbon at $E_\nu \sim 3.5$ GeV', *Phys. Rev. Lett.* **111**, 022501.

[32] Filkins, A. et al. 2016, 'Measurement of Muon Neutrino and Antineutrino Inclusive Charged-Current Cross Sections in the Low-A Energy Range', *Phys. Rev. D* **94**, 092005.

[33] Fiorentini, G. A. et al. 2013, 'Measurement of Muon Neutrino Quasi-Elastic Scattering on a Hydrocarbon Target at $E_\nu \sim 3.5$ GeV', *Phys. Rev. Lett.* **111**, 022502.

[34] Formaggio, J. A. and Zeller, G. P. 2012, 'From eV to EeV: Neutrino Cross Sections Across Energy Scales', *Rev. Mod. Phys.* **84**, 1307–1341.

[35] Frühwirth, R. 1987, 'Application of kalman filtering to track and vertex fitting', *Nucl. Instrum. Meth. A* **262**, 444–450.

[36] Fukuda, Y. et al. 1998, 'Evidence for oscillation of atmospheric neutrinos', *Phys. Rev. Lett.* **81**(8), 1562–1567.

[37] Higuera, A. et al. 2014, 'Measurement of Coherent Production of $\pi^{\pm}$ in Neutrino and Antineutrino Beams on Carbon from E_ν of 1.5 to 20 GeV', *Phys. Rev. Lett.* **113**, 261802.

[38] Hough, P. V. C. 1959, Machine analysis of bubble chamber pictures, *in* 'Proc. Int. Conf. High Energy Accelerators and Instrumentation', CERN, Geneva, p. 554.

[39] Kabirnezhad, M. 2018, 'Single Pion Production in Neutrino-Nucleon Interactions', *Phys. Rev. D* **97**(1), 013002.

[40] Katori, T. and Martini, M. 2016, 'Neutrino-nucleus cross sections for oscillation experiments'.

URL: *https://arxiv.org/abs/1611.07770*

[41] Knuth, D. E. 1968, 'Semantics of context-free languages', *Mathematical Systems Theory* **2**(2), 127–145.

[42] Llewellyn Smith, C. 1972, 'Neutrino reactions at accelerator energies', *Physics Reports* **3**(5), 261–379.

URL: *https://www.sciencedirect.com/science/article/pii/0370157372900105*

[43] Lyubushkin, V. et al. 2009, 'A Study of quasi-elastic muon neutrino and antineutrino scattering in the NOMAD experiment', *Eur. Phys. J. C* **63**, 355–381.

[44] Martini, M., Ericson, M., Chanfray, G. and Marteau, J. 2009*a*, 'A Unified approach for nucleon knock-out, coherent and incoherent pion production in neutrino interactions with nuclei', *Phys. Rev. C* **80**, 065501.

[45] Martini, M., Ericson, M., Chanfray, G. and Marteau, J. 2009*b*, 'Unified approach for nucleon knock-out and coherent and incoherent pion production in neutrino interactions with nuclei', *Physical Review C* **80**(6).

URL: *http://dx.doi.org/10.1103/PhysRevC.80.065501*

[46] Megias, G. D., Bolognesi, S., Barbaro, M. B. and Tomasi-Gustafsson, E. 2020, 'New evaluation of the axial nucleon form factor from electron- and neutrino-scattering data and impact on neutrino-nucleus cross sections', *Phys. Rev. C* **101**(2), 025501.

[47] Messerly, B. 2019, Single Charged Pion Production by Muon Neutrinos in the MINERvA Detector Using the NuMI Beam, PhD thesis, Pittsburgh U.

[48] Messerly, B. et al. 2021, 'An error analysis toolkit for binned counting experiments', *EPJ Web Conf.* **251**, 03046.

[49] Meyer, A. S., Walker-Loud, A. and Wilkinson, C. 2022, 'Status of Lattice QCD Determination of Nucleon Form Factors and their Relevance for the Few-GeV Neutrino Program', *Ann. Rev. Nucl. Part. Sci.* **72**, 205–232.

[50] Navas, S. et al. 2024, 'Review of particle physics', *Phys. Rev. D* **110**, 030001.

URL: *https://link.aps.org/doi/10.1103/PhysRevD.110.030001*

[51] Nieves, J., Simo, I. R. and Vacas, M. J. V. 2011, 'Inclusive charged-current neutrino-nucleus reactions', *Physical Review C* **83**(4).

URL: *http://dx.doi.org/10.1103/PhysRevC.83.045501*

[52] Patrick, C. E. et al. 2019, 'Measurement of Single Charged Pion Production in ν_μ Charged-Current Interactions on Hydrocarbon with the MINERvA Detector', *Phys. Rev. D* **99**(1), 012004.

[53] Patrick, C. E. et al. 2020, 'Measurement of transverse kinematic imbalance in neutrino-muon proton production on hydrocarbon at $\langle E\nu \rangle \sim 3$ gev', *Phys. Rev. D* **101**(9), 092001.

[54] Patrick, C. and others (MINERvA Collaboration) 2018, 'Measurement of quasielasticlike neutrino scattering at $\langle E\nu \rangle \approx 3.5$ gev on hydrocarbon at minerva', *Phys. Rev. D* **97**, 052002.

[55] Rein, D. and Sehgal, L. M. 1981, 'Neutrino-excitation of baryon resonances and single pion production', *Annals of Physics* **133**(1), 79–153.

URL: *https://www.sciencedirect.com/science/article/pii/0003491681902426*

[56] Schiavilla, R., Wiringa, R. B., Pieper, S. C. and Carlson, J. 2007, 'Tensor Forces and the Ground-State Structure of Nuclei', *Phys. Rev. Lett.* **98**, 132501.

[57] Schwehr, J., Cherdack, D. and Gran, R. 2016, 'GENIE implementation of IFIC Valencia model for QE-like 2p2h neutrino-nucleus cross section'.

[58] Shiltsev, V. 2017, 'Fermilab proton accelerator complex status and improvement plans', *Modern Physics Letters A* **32**(16), 1730012.

URL: *http://dx.doi.org/10.1142/S0217732317300129*

[59] Smith, R. and Moniz, E. 1972, 'Neutrino reactions on nuclear targets', *Nuclear Physics B* **43**, 605–622.

URL: *https://www.sciencedirect.com/science/article/pii/0550321372900405*

[60] Sobczyk, J. T. 2012, 'Multinucleon Ejection Model for Meson Exchange Current Neutrino Interactions', *Phys. Rev. C* **86**, 015504.

[61] Tagg, N., Brangham, J., Chvojka, J., Clairemont, M., Day, M., Eberly, B., Felix, J., Fields, L., Gago, A., Gran, R., Harris, D., Kordosky, M., Lee, H., Maggi, G., Maher, E., Mann, W., Marshall, C., McFarland, K., McGowan, A., Mislivec, A., Mousseau, J., Osmanov, B., Osta, J., Paolone, V., Perdue, G., Ransome, R., Ray, H., Schellman, H., Schmitz, D., Simon, C., Solano Salinas, C., Tice, B., Walding, J., Walton, T., Wolcott, J., Zhang, D. and Ziemer, B. 2012, 'Arachne—a web-based event viewer for', *Nuclear Instruments and Methods in Physics Research Section A: Accelerators, Spectrometers, Detectors and Associated Equipment* **676**, 44–49.

URL: *http://dx.doi.org/10.1016/j.nima.2012.01.059*

[62] Tice, B. 2017, 'Minerva results and future prospects', Talk at NuFact 2017, Uppsala University. Slides available at https://indico.uu.se/event/324/contributions/339/attachments/551/680/NUFACT_2017_v04.pdf.

[63] Walton, T. et al. 2015, 'Proton and Muon Kinematics in Quasielastic-like ν_μ-Hydrocarbon Interactions in MINERvA', *Phys. Rev. D* **91**, 071301.

[64] Whitlow, L. W., Riordan, E. M., Dasu, S., Rock, S. and Bodek, A. 1992, 'Precise measurements of the proton and deuteron structure functions from a global analysis of the SLAC deep inelastic electron scattering cross-sections', *Phys. Lett. B* **282**, 475–482.

[65] Wolcott, J. 2015, 'Electron neutrino charged-current quasielastic scattering in the minerva experiment'.

URL: *https://arxiv.org/abs/1510.08342*